

Dynamic fingerprint of fractionalized excitations in single-crystalline $\text{Cu}_3\text{Zn}(\text{OH})_6\text{FBr}$

Ying Fu,^{1,*} Miao-Ling Lin,^{2,3,*} Le Wang,¹ Qiye Liu,¹ Lianglong Huang,¹ Wenrui Jiang,¹ Zhanyang Hao,¹ Cai Liu,¹ Hu Zhang,⁴ Xingqiang Shi,⁴ Jun Zhang,^{2,3} Junfeng Dai,¹ Dapeng Yu,¹ Fei Ye,^{1,5} Patrick A. Lee,⁶ Ping-Heng Tan,^{2,3,†} and Jia-Wei Mei^{1,5,‡}

¹*Shenzhen Institute for Quantum Science and Engineering, and Department of Physics, Southern University of Science and Technology, Shenzhen 518055, China*

²*State Key Laboratory of Superlattices and Microstructures, Institute of Semiconductors, Chinese Academy of Sciences, Beijing 100083, China*

³*Center of Materials Science and Optoelectronics Engineering & CAS Center of Excellence in Topological Quantum Computation, University of Chinese Academy of Sciences, 100049 Beijing, China*

⁴*College of Physics Science and Technology, Hebei University, Baoding 071002, China*

⁵*Shenzhen Key Laboratory of Advanced Quantum Functional Materials and Devices, Southern University of Science and Technology, Shenzhen 518055, China*

⁶*Department of Physics, Massachusetts Institute of Technology, Cambridge, Massachusetts 02139, USA*
(Dated: October 16, 2020)

Quantum spin liquid (QSL) represents a new class of condensed matter states characterized by the long-range many-body entanglement of topological orders. The most prominent feature of the elusive QSL state is the existence of fractionalized spin excitations. Subject to the strong quantum fluctuations, the spin-1/2 antiferromagnetic system on a kagome lattice is the promising candidate for hosting a QSL ground state, but the structurally ideal realization is rare. Here, we report Raman scattering measurements on the single crystalline $\text{Cu}_3\text{Zn}(\text{OH})_6\text{FBr}$, and confirm that the ideal kagome structure remains down to low temperatures without any lattice distortion by the angle-resolved polarized Raman responses and second-harmonic-generation measurements. Furthermore, at low temperatures the Raman scattering reveals a continuum of the spin excitations in $\text{Cu}_3\text{Zn}(\text{OH})_6\text{FBr}$, in contrast to the sharp magnon peak in the ordered kagome antiferromagnet $\text{EuCu}_3(\text{OH})_6\text{Cl}_3$. Such magnetic Raman continuum, in particular, the substantial low-energy one-pair spinon excitation serves as strong evidence for fractionalized spin excitations in $\text{Cu}_3\text{Zn}(\text{OH})_6\text{FBr}$.

I. INTRODUCTION

When subject to strong quantum fluctuation and geometrical frustration, the quantum spin system may not develop into a magnetically ordered state[1, 2], but a quantum spin liquid (QSL) ground state at zero temperature.[3–6] QSL has no classic counterpart as it exhibits various topological orders characterized by the long-range entanglement pattern.[7–9] The lattice of the spin-1/2 kagome network of corner-sharing triangles is a long-sought platform for antiferromagnetically interacting spins to host a QSL ground state.[10–16] Herbersmithite [$\text{ZnCu}_3(\text{OH})_6\text{Cl}_2$] is the first promising kagome QSL candidate,[3, 16–23] in which no long-range magnetic order was detected down to low temperature,[17, 18] and inelastic neutron scattering on single crystals revealed a magnetic continuum, as a hallmark of fractionalized spin excitations.[20, 22] Up to date, most, if not all, experimental information on the nature of kagome QSL relies on a single compound of Herbersmithite. Considering the fact that a lattice distortion away from a perfect kagome structure has recently been confirmed in Herbersmithite,[24, 25] which stimulates investigations on the subtle magneto-elastic effect in the kagome materials,[26, 27] an alternative realization of the QSL compound with the ideal kagome lattice is still in urgent need. Zn-Barlowite [$\text{Cu}_3\text{Zn}(\text{OH})_6\text{FBr}$] is such a can-

didate for a kagome QSL ground state [28–38] with no lattice distortion being reported yet. Measurements on the powder samples of Zn-Barlowite indicate the absence of long-range magnetic order or spin freezing down to temperatures of 0.02 K, four orders of magnitude lower than the Curie-Weiss temperature.[30, 32] Besides the absence of long-range magnetic order down to low temperature, the fractionalized spin excitations, i.e. spinons, in the spectroscopy is essential evidence for the long-range entanglement pattern in QSL. However, spectroscopic evidence for the deconfined spinon excitations in Zn-Barlowite is still lacking, in part due to unavailable single-crystal samples. Note that for Zn-Barlowite $\text{Cu}_{4-x}\text{Zn}_x(\text{OH})_6\text{FBr}$ the doping parameter $x \leq 0.56$, in the previously reported Zn-Barlowite single crystal samples, does not belong to the QSL regime.[33–35, 37, 38]

In this work, we report the synthesis of the single crystals of $\text{Cu}_{4-x}\text{Zn}_x(\text{OH})_6\text{FBr}$ ($x = 0.82$) of millimeter size, which is in the QSL regime, and the spin dynamics revealed by the inelastic light scattering on these samples. We confirm the ideal kagome-lattice structure by the angle-resolved polarized Raman responses and second-harmonic-generation (SHG), and observe a magnetic Raman continuum in our crystal samples. Raman scattering has previously been reported for Herbersmithite,[19] and the overall continuum agreed with that in Zn-Barlowite. Although it was not discussed, the lattice distortion in Herbersmithite was evident by the anisotropic angle dependent Raman responses [19] and may account for the difference from our results in details. In the theory the Raman spectrum of the kagome QSL contains the one-pair component of spinon-antispinon

* These two authors contributed equally.

† phtan@semi.ac.cn

‡ meijw@sustech.edu.cn

excitations with a peculiar power-law behavior at low frequency, serving as the fingerprint of spinons.[39] Our measured magnetic Raman continuum agrees well with the theoretical prediction, revealing the fractionalized spin excitation in $\text{Cu}_{3.18}\text{Zn}_{0.82}(\text{OH})_6\text{FBr}$.

To demonstrate the one-pair spinon dynamics in the kagome QSL even more evidently, we perform a control experiment on a kagome antiferromagnet $\text{EuCu}_3(\text{OH})_6\text{Cl}_3$, which suffers a spinon confinement as a transition taking places from a paramagnetic phase to a $\mathbf{q} = 0$ type 120° non-collinear antiferromagnetic order (AFM) ground state below the Néel temperature $T_N = 17$ K.[40–42] We observe a magnon peak in the AFM state, which can be regarded as the spinon confinement in the magnetically ordered state as schematically summarized in Fig. 1. The magnon excitation emerges from the one-pair continuum, firstly reported in our work, and can be regarded as the bound state of the spinon-antispinon excitations.

II. RESULTS

We synthesized single crystals of Barlowite $\text{Cu}_4(\text{OH})_6\text{FBr}$, Zn-Barlowite $\text{Cu}_{3.18}\text{Zn}_{0.82}(\text{OH})_6\text{FBr}$, and $\text{EuCu}_3(\text{OH})_6\text{Cl}_3$ (we use the short-hand notation Cu4, Cu3Zn, and EuCu3, respectively) with high quality (Methods and Supplementary Section1). The crystal structure of Cu3Zn was determined by the single-crystal X-ray diffraction, and chemical analysis (ICP-AES) indicated the crystal composition is $\text{Cu}_{3.18}\text{Zn}_{0.82}(\text{OH})_6\text{FBr}$ (Methods), in the QSL region of the magnetic phase diagram.[37, 38] The interlayer Cu^{2+} concentration (18%) is comparable to that (15%) in Herbertsmithite.[43] The crystal structure of Cu4 coincides with Barlowite 1 in Refs. [34, 35]. We fit the high-temperature magnetic susceptibility (Supplementary Section1) by the Curie-Weiss behavior to estimate the superexchange strength for the Cu^{2+} spin-1/2 moments on the kagome lattice in Cu3Zn, $J \simeq 19$ meV ($\Theta_{\text{CW}} = -220$ K). The antiferromagnetic super-exchange interaction for EuCu3 is about $J \simeq 10$ meV.[40–42] Note the electronic ground state of Eu^{3+} in EuCu3 is the non-magnetic 7F_0 configuration.

To study changes in the crystal structures of Cu3Zn and Cu4, we track the temperature evolution of Raman spectra in the two compounds. Cu3Zn and Cu4 at high temperature crystallize the same space group $P6_3/mmc$. [28, 30] We didn't observe the structural phase transition in Cu3Zn from the Raman scattering down to low temperature (Supplementary Section2 and 3). Cu4 transforms to orthorhombic $Pnma$ below 265 K, characterized by changes in the relative occupancies of the interlayer Cu^{2+} site.[31, 33–35] The splitting of phonon peaks in Cu4 due to the superlattice folding in the orthorhombic $Pnma$ phase is resolved for several modes [Supplementary Fig.S4]. Cu3Zn displays sharp E_{2g} modes at 125 cm^{-1} for in-plane relative movements of Zn^{2+} . The corresponding modes for the interlayer Cu^{2+} in Cu4 are broad at 290 K due to the randomly distributed interlayer Cu^{2+} and split into two peaks below the structural transition temperature. Cu3Zn has no Raman-active mode related to the kagome Cu^{2+} vibra-

tions, indicating the kagome layer remains substantially intact as the inversion center of Cu^{2+} sites is evident. The kagome layers in Cu4 are distorted, signaled by a new phonon mode for the kagome Cu^{2+} vibration at 62 cm^{-1} . Besides sharp phonon modes, we observe a Raman continuum background in Cu3Zn, particularly at low frequency, signifying substantial magnetic excitations.

Previous X-ray and neutron refinements of the crystal structure suggest ideal kagome planes in Cu3Zn. SHG confirmed the parity symmetry of the crystallographic structure in Barlowite 2 $\text{Cu}_4(\text{OH})_6\text{FBr}$ and Zn-Barlowite $\text{Cu}_{3.66}\text{Zn}_{0.33}(\text{OH})_6\text{FBr}$. In Supplementary Section7, we also reveal the inversion symmetry by SHG in our single crystals of Cu3Zn. To further exclude subtle local symmetry lowering or lattice distortions, we perform the angle-resolved polarization-dependent Raman measurements of Cu3Zn for magnetic and lattice vibration modes.[44, 45] The threefold rotation symmetry of the kagome lattice leads to isotropic angle dependence in the XX configuration both for A_{1g} and E_{2g} components, XY and X -only configurations for the E_{2g} component; it also gives rise to the angle θ dependence of $\cos^2 \theta$ in the X -only configuration for the A_{1g} component. We find that the angle dependence of Raman responses, in particular for the magnetic continuum at low frequency, the $\text{Br}^- E_{2g}$ phonon, and $\text{O}^{2-} A_{1g}$ phonon modes, fit the theoretical curves very well [Supplementary Section4], confirming the threefold rotational symmetry of the kagome lattice in the dynamical Raman responses of the lattice vibrations and magnetic excitations. Combining the X-ray and neutron refinement,[30–32, 38] we conclude that Cu3Zn manifests a structurally ideal realization of layered spin-1/2 Cu^{2+} kagome-lattice planes.

Having established the absence of a sharp anomaly in the thermodynamic properties [Supplementary Section1] and the lack of an emergent magnetic order with the weak symmetry breaking in the angle-dependent polarized Raman response, which is the first step to a QSL, we now present our main results of the magnetic Raman continuum in Cu3Zn with subtracting phonon contribution, as shown in Fig. 2. The susceptibility is related to the Raman intensity $I(\omega) = (1 + n(\omega))\chi''(\omega)$ with the bosonic temperature factor $n(\omega)$. Fig. 2a, b and c are the A_{1g} magnetic Raman response in Cu3Zn, which measures the thermal fluctuation of the interacting spins on the kagome lattice.[46–48] We can see that the A_{1g} channel is activated only at high temperatures, disappears at low temperatures, behaving as the thermally activated excitations. At high temperatures, the Raman spectra exhibit the quasielastic scattering that is common in the inelastic light scattering for the spin systems.[48] The maximum in the Raman response function decreases from 60 cm^{-1} at room temperature to 30 cm^{-1} at 110 K , and the magnetic intensity becomes hardly resolved at low temperatures below 50 K . The integrated Raman susceptibility $\chi'_{A_{1g}}(T)$ in Fig. 2b fits the thermally activated function, $\propto e^{-\omega^*/T}$ with $\omega^* = 53 \text{ cm}^{-1}$, different from the power-law temperature dependence of the quasielastic scattering in Herbertsmithite.[19] The temperature dependence of the A_{1g} magnetic Raman susceptibilities $\chi''_{A_{1g}}(\omega, T)$ in Cu3Zn distributes the main spectral weight among the frequency region less than 400 cm^{-1} and the tem-

perature range above 50 K in Fig. 2c.

Different from the A_{1g} channel, the pronounced E_{2g} magnetic Raman continuum in Cu3Zn persists at low temperatures (Fig. 2d), indicating the quantum fluctuation of the kagome spin-1/2 system. Along with the theoretical work,[39] we schematically decompose the E_{2g} Raman continuum into two components, which have the maximum around 150 cm^{-1} and the higher one around 400 cm^{-1} , respectively. We denote them as spin excitations for one spin-antispinon pair (one-pair) and two spinon-antispinon pair (two-pair) excitations, respectively.[39] Like the two-magnon scattering in the antiferromagnet,[48, 49] the two-pair component doesn't show a significantly non-monotonic temperature dependence as reducing temperatures. The substantial low energy one-pair component has a more pronounced non-monotonic temperature dependence. It increases with the temperature decreasing from 290 K to 50 K and decreases with further temperature reduce as shown in Figs. 2d, e, and f. The frequency and temperature dependence of the E_{2g} magnetic Raman susceptibilities $\chi''_{E_{2g}}(\omega, T)$ distributes the main spectral weight among the frequency region less than 400 cm^{-1} , and reaches the maximum at around 150 cm^{-1} and 50 K, as shown in Fig. 2f. We also observed the Fano effect for the E_{2g} F^- phonon peak at 173 cm^{-1} in Cu3Zn [Supplementary Section3], whose asymmetric lineshape provides an additional probe of the magnetic continuum.

The one-pair component in the E_{2g} Raman continuum is crucial as it has an origin in the spinon excitation in the kagome QSL from the perspective of theory.[39] With the incoming and outgoing light polarizations \hat{e}_{in} and \hat{e}_{out} , magnetic Raman scattering measures the spin-pair (two-spin-flip) dynamics in terms of the Raman tensor[39, 44, 50, 51]

$$\tau_R = \sum_{\langle ij \rangle} (\hat{e}_{\text{in}} \cdot \mathbf{r}_{ij})(\hat{e}_{\text{out}} \cdot \mathbf{r}_{ij}) \mathbf{S}_i \cdot \mathbf{S}_j, \quad (1)$$

where the summation runs over $\langle ij \rangle$ for the nearest neighbor bonds \mathbf{r}_{ij} for the \mathbf{S}_i and \mathbf{S}_j on the kagome lattice. At zero temperature, the magnetic Raman susceptibility is given as $\chi''_R(\omega) = \sum_f |\langle f | \tau_R | 0 \rangle|^2 \delta(\omega - \omega_f) = \sum_f \mathcal{M}_f^R(\omega_f) \delta(\omega - \omega_f) \simeq M(\omega) \mathcal{D}(\omega)$, in which we set the ground state energy to be zero. $\mathcal{M}_f^R(\omega_f) = |\langle f | \tau_R | 0 \rangle|^2$ denotes the matrix element for the transition between the ground state $|0\rangle$ and the excited state $|f\rangle$. $M(\omega) = \sum_{f: \omega_f = \omega} \mathcal{M}_f^R = \overline{\mathcal{M}}_f^R(\omega_f)$ is the average matrix element, and $\mathcal{D}(\omega) = \sum_{f: \tau_R \text{ allowed final states}} \delta(\omega - \omega_f)$ denotes the density of state (DOS) for the Raman tensor associated excitations. Introducing the spinon operator $f_{i\sigma}$ in QSL, the spin-pair operator in the Raman tensor is rewritten in terms of two pairs of spinon-antispinon excitations $\tau_R \propto f_{i\sigma}^\dagger f_{j\sigma} f_{j\sigma'}^\dagger f_{i\sigma'}$. Besides the two-pair excitation, the magnetic Raman continuum contains the one-pair spinon excitation as $\tau_R \propto \chi (f_{i\sigma}^\dagger f_{j\sigma} + f_{j\sigma}^\dagger f_{i\sigma})$, where $\chi = \langle f_{i\sigma}^\dagger f_{j\sigma} \rangle$ is the spinon mean-field hopping amplitude.[39] As shown in Fig. 2d, the one-pair component in the measured Raman susceptibility in the E_{2g} has the maximum at 150 cm^{-1} (J), and extends up to 400 cm^{-1} ($2.6J$) at low temperatures. The two-pair component has the maximum at 400 cm^{-1} ($2.6J$) and the cut-off around 750 cm^{-1} ($4.9J$). In totality, the mentioned

features (maxima and cut-offs) of one- and two-pair excitations in the E_{2g} measured Raman response in Cu3Zn (Fig. 2d) overall agree well with the theoretical calculation for the kagome QSL state.[39]

In more detail, the one-pair component dominates the E_{2g} magnetic Raman continuum at low frequency. It displays the power-law behavior up to 70 cm^{-1} , with a significantly non-monotonic temperature dependence, as shown in Figs. 3. As lowering the temperature, the E_{2g} continuum at low frequency increases above 50 K and decreases below 50 K. The low-energy continuum evolves from a sublinear behavior T^α with $\alpha < 1$ to a superlinear one T^α with $\alpha > 1$ as reducing the temperature. A central question for the kagome spin liquid is whether a spin gap exist. The results of the spin gap in Herbertsmithite are controversial due to the difficulty of singling out the kagome susceptibility.[21, 23] Previous results on the powder samples of Cu3Zn suggest a small spin gap.[30, 32] and measurements on the single-crystal samples would be of great interest. If such a gap exists, the power-law behavior of the E_{2g} magnetic Raman continua sets an upper bound for the spin gap of 2 meV.

The temperature-dependent magnetic continua of Cu3Zn in Figs. 2d, e, and f, and Fig. 3 imply the maximal spin fluctuations at the characteristic temperature 50 K. The maximum of the kagome spin fluctuations in Cu3Zn signifies the spin singlet forming,[2, 52] but is masked by the inter-layer Cu^{2+} moments in the thermodynamic properties [Supplementary Section1]. It can be revealed by the Knight shift related to the kagome spins in the nuclear magnetic resonance measurements.[30] In contrast to significant energy dependence in magnetic Raman continuum in Cu3Zn in Figs. 2 and 3, the scattered neutron signal in Herbertsmithite is overall insensitive to energy transfer, rather flat above 1.5 meV, but increases significantly at low-energy scattering due to the interlayer Cu^{2+} ions.[20, 22] The interlayer Cu^{2+} ions distribute spatially away from each other, and the spin-pair magnitude among themselves and between them and kagome spins is weak, giving rise to a negligible matrix element in Raman tensors. So different from the neutron scattering, the Raman scattering is not sensitive to the inter-layer Cu^{2+} at low energies, advantageous to the detection of kagome spins. Furthermore, inelastic neutron scattering in Herbertsmithite measures the magnetic continuum up to 2-3 J ,[20] the same energy range as the one-pair Raman component in Cu3Zn. These results suggest that the magnetic Raman continuum originates from the kagome-plane spins, and the one-pair component has an origin of spinon excitations.

The theoretical calculation for kagome Dirac spin liquid (DSL) predicts the power-law behavior for the Raman susceptibility in the E_{2g} channel at low frequency.[39] The one-pair spinon excitation in DSL gives the linear density of state $\mathcal{D}_{\text{IP}} \propto \omega$. The matrix element turns out to be exactly zero for all one-pair excitations in the mean field Dirac Hamiltonian. As a result a Raman spectrum that scales as ω^3 was predicted.[39] However, the vanishing of the matrix element is somewhat accidental and depends on the assumption of a DSL in a Heisenberg model in an ideal kagome lattice. Any deviation from the ideal DSL state, *e.g.* a small gap in

the ground state,[30, 32] DM interactions, or other effects of perturbations,[26, 53] changes the wave functions and may result in a constant matrix element $M(\omega)$. In that case, the Raman spectrum will be simply proportional to the DOS of the one-pair component \mathcal{D}_{1P} which is linear in ω . From our fitting for Cu3Zn in Fig. 3, we find that $\alpha = 1.3$ when approaching zero temperature. The existence of a small gap in the spinon spectrum may explain this discrepancy. We also note that according to the theory [39] the A_{1g} and A_{2g} contributions to the one-pair continuum are the forth-order effect, much smaller than the E_{2g} contributions. This explains the invisible one-pair continuum in the A_{1g} and A_{2g} channels.

Figure 4 presents a control Raman study on the magnetic ordered kagome antiferromagnet EuCu3, which has the antiferromagnetic superexchange $J \simeq 10$ meV, half of the value in Cu3Zn. EuCu3 belongs to the atacamite family with the perfect kagome lattice and has the $\mathbf{q} = 0$ type 120° ordered spin configuration below T_N due to a large Dzyaloshinski-Moriya (DM) interaction [Supplementary Section8].[40, 42, 54–56] Above the ordering temperature $T_N = 17$ K, the magnetic Raman continuum in the E_g channel displays the extended continuum, similar to that in Zn-Barlowite at 4 K as shown in Fig.S10 in Supplementary Section6. This indicates the strong magnetic fluctuations in EuCu3. The less pronounced low-energy continuum excitations in EuCu₃(OH)₆Cl₃ indicate the suppression of the quantum fluctuation due to a large DM interaction. The low energy excitation in the ordered state is the spin-wave excitation, i.e. magnon, and the E_g Raman scatter-

ing measures one- and two-magnon excitations for the non-collinear 120° spin configuration as detailed in the Methods section, leading to a sharp magnon peak at 72 cm^{-1} superimposing on the two-magnon continuum. In this sense, the AFM transition may be thought of as a confinement transition. The comparative studies between Cu3Zn and EuCu3 are sketched in Fig. 1, demonstrating the spinon deconfinement and confinement, respectively, in the different ground states.

III. CONCLUSIONS

Our Raman scattering studies compare the spin dynamics in the kagome QSL compound Cu3Zn and magnetically ordered antiferromagnet EuCu3. In contrast to a sharp magnon peak in EuCu3, the overall magnetic Raman scattering in Cu3Zn agrees well with the theoretical prediction for a spin liquid state. The spinon continuum is evident, providing the strongest evidence yet for the kagome QSL ground state in Cu3Zn. On the material side, Zn-Barlowite provides an ideal structural realization of the kagome lattice, and the available single crystal samples stimulate future systematical studies of the kagome QSL. Along with Herbertsmithite, the single-crystalline Zn-Barlowite stands able to provide considerable insight into singling out the intrinsic properties of the intrinsic nature of the kagome QSL, without deceiving by the material chemistry details.

-
- [1] P. W. Anderson, Resonating valence bonds: A new kind of insulator?, *Materials Research Bulletin* **8**, 153 (1973).
- [2] P. W. Anderson, The Resonating Valence Bond State in La_2CuO_4 and Superconductivity., *Science* **235**, 1196 (1987).
- [3] P. A. Lee, An end to the drought of quantum spin liquids, *Science* **321**, 1306 (2008).
- [4] L. Balents, Spin liquids in frustrated magnets, *Nature* **464**, 199 (2010).
- [5] Y. Zhou, K. Kanoda, and T.-K. Ng, Quantum spin liquid states, *Rev. Mod. Phys.* **89**, 025003 (2017).
- [6] C. Broholm, R. J. Cava, S. A. Kivelson, D. G. Nocera, M. R. Norman, and T. Senthil, Quantum spin liquids, *Science* **367**, 10.1126/science.aay0668 (2020).
- [7] A. Kitaev and J. Preskill, Topological entanglement entropy, *Phys. Rev. Lett.* **96**, 110404 (2006).
- [8] M. Levin and X.-G. Wen, Detecting Topological Order in a Ground State Wave Function, *Phys. Rev. Lett.* **96**, 110405 (2006).
- [9] X.-G. Wen, Choreographed entanglement dances: Topological states of quantum matter, *Science* **363**, 10.1126/science.aal3099 (2019).
- [10] Y. Ran, M. Hermele, P. A. Lee, and X.-G. Wen, Projected-wave-function study of the spin-1/2 heisenberg model on the kagomé lattice, *Phys. Rev. Lett.* **98**, 117205 (2007).
- [11] M. Hermele, Y. Ran, P. A. Lee, and X.-G. Wen, Properties of an algebraic spin liquid on the kagome lattice, *Phys. Rev. B* **77**, 224413 (2008).
- [12] S. Yan, D. A. Huse, and S. R. White, Spin-Liquid Ground State of the $S = 1/2$ Kagome Heisenberg Antiferromagnet, *Science* **332**, 1173 (2011).
- [13] H.-C. Jiang, Z. Wang, and L. Balents, Identifying topological order by entanglement entropy, *Nat Phys* **8**, 902 (2012).
- [14] M. P. Zaletel and A. Vishwanath, Constraints on topological order in mott insulators, *Phys. Rev. Lett.* **114**, 077201 (2015).
- [15] J.-W. Mei, J.-Y. Chen, H. He, and X.-G. Wen, Gapped spin liquid with \mathbb{Z}_2 topological order for the kagome Heisenberg model, *Phys. Rev. B* **95**, 235107 (2017).
- [16] M. R. Norman, *Colloquium* : Herbertsmithite and the search for the quantum spin liquid, *Rev. Mod. Phys.* **88**, 041002 (2016).
- [17] M. P. Shores, E. A. Nytko, B. M. Bartlett, and D. G. Nocera, A structurally perfect $S = 1/2$ kagome antiferromagnet, *Journal of the american chemical society* **127**, 13462 (2005).
- [18] P. Mendels, F. Bert, M. A. de Vries, A. Olariu, A. Harrison, F. Duc, J. C. Trombe, J. S. Lord, A. Amato, and C. Baines, Quantum magnetism in the paratacamite family: Towards an ideal kagomé lattice, *Phys. Rev. Lett.* **98**, 077204 (2007).
- [19] D. Wulferding, P. Lemmens, P. Scheib, J. Röder, P. Mendels, S. Chu, T. Han, and Y. S. Lee, Interplay of thermal and quantum spin fluctuations in the kagome lattice compound herbertsmithite, *Phys. Rev. B* **82**, 144412 (2010).
- [20] T.-H. Han, J. S. Helton, S. Chu, D. G. Nocera, J. A. Rodriguez-Rivera, C. Broholm, and Y. S. Lee, Fractionalized excitations in the spin-liquid state of a kagome-lattice antiferromagnet, *Nature* **492**, 406 (2012).
- [21] M. Fu, T. Imai, T.-H. Han, and Y. S. Lee, Evidence for a gapped spin-liquid ground state in a kagome heisenberg antiferromagnet, *Science* **350**, 655 (2015).

- [22] T.-H. Han, M. R. Norman, J.-J. Wen, J. A. Rodriguez-Rivera, J. S. Helton, C. Broholm, and Y. S. Lee, Correlated impurities and intrinsic spin-liquid physics in the kagome material herbertsmithite, *Phys. Rev. B* **94**, 060409 (2016).
- [23] P. Khuntia, M. Velazquez, Q. Barthélemy, F. Bert, E. Kermarrec, A. Legros, B. Bernu, L. Messio, A. Zorko, and P. Mendels, Gapless ground state in the archetypal quantum kagome antiferromagnet $\text{ZnCu}_3(\text{OH})_6\text{Cl}_2$, *Nature Physics* **16**, 469 (2020).
- [24] A. Zorko, M. Herak, M. Gomilšek, J. van Tol, M. Velázquez, P. Khuntia, F. Bert, and P. Mendels, Symmetry reduction in the quantum kagome antiferromagnet herbertsmithite, *Phys. Rev. Lett.* **118**, 017202 (2017).
- [25] N. J. Laurita, A. Ron, J. W. Han, A. Scheie, J. P. Sheckelton, R. W. Smaha, W. He, J. J. Wen, J. S. Lee, Y. S. Lee, M. R. Norman, and D. Hsieh, Evidence for a parity broken monoclinic ground state in the $s = 1/2$ kagomé antiferromagnet herbertsmithite (2019), [arXiv:1910.13606 \[cond-mat.str-el\]](https://arxiv.org/abs/1910.13606).
- [26] M. R. Norman, N. J. Laurita, and D. Hsieh, Valence bond phases of herbertsmithite and related copper kagome materials, *Phys. Rev. Research* **2**, 013055 (2020).
- [27] Y. Li, A. Pustogow, M. Bories, P. Puphal, C. Krellner, M. Dressel, and R. Valentí, Lattice dynamics in the spin- $\frac{1}{2}$ frustrated kagome compound herbertsmithite, *Phys. Rev. B* **101**, 161115 (2020).
- [28] T.-H. Han, J. Singleton, and J. A. Schlueter, Barlowite: A Spin- $1/2$ Antiferromagnet with a Geometrically Perfect Kagome Motif, *Phys. Rev. Lett.* **113**, 227203 (2014).
- [29] Z. Liu, X. Zou, J.-W. Mei, and F. Liu, Selectively doping barlowite for quantum spin liquid: A first-principles study, *Phys. Rev. B* **92**, 220102 (2015).
- [30] Z. Feng, Z. Li, X. Meng, W. Yi, Y. Wei, J. Zhang, Y.-C. Wang, W. Jiang, Z. Liu, S. Li, F. Liu, J. Luo, S. Li, G. Qing Zheng, Z. Y. Meng, J.-W. Mei, and Y. Shi, Gapped Spin- $1/2$ Spinon Excitations in a New Kagome Quantum Spin Liquid Compound $\text{Cu}_3\text{Zn}(\text{OH})_6\text{FBr}$, *Chinese Physics Letters* **34**, 077502 (2017).
- [31] Z. Feng, Y. Wei, R. Liu, D. Yan, Y.-C. Wang, J. Luo, A. Senyshyn, C. d. Cruz, W. Yi, J.-W. Mei, Z. Y. Meng, Y. Shi, and S. Li, Effect of Zn doping on the antiferromagnetism in kagome $\text{Cu}_{4-x}\text{Zn}_x(\text{OH})_6\text{FBr}$, *Phys. Rev. B* **98**, 155127 (2018).
- [32] Y. Wei, Z. Feng, W. Lohstroh, C. dela Cruz, W. Yi, Z. F. Ding, J. Zhang, C. Tan, L. Shu, Y.-C. Wang, J. Luo, J.-W. Mei, Z. Y. Meng, Y. Shi, and S. Li, Evidence for a Z_2 topological ordered quantum spin liquid in a kagome-lattice antiferromagnet (2017), [arXiv:1710.02991](https://arxiv.org/abs/1710.02991).
- [33] C. Pasco, B. Trump, T. T. Tran, Z. Kelly, C. Hoffmann, I. Heinmaa, R. Stern, and T. McQueen, Single-crystal growth of $\text{Cu}_4(\text{OH})_6\text{BrF}$ and universal behavior in quantum spin liquid candidates synthetic barlowite and herbertsmithite, *Physical Review Materials* **2**, 044406 (2018).
- [34] R. W. Smaha, W. He, J. P. Sheckelton, J. Wen, and Y. S. Lee, Synthesis-dependent properties of barlowite and Zn-substituted barlowite, *Journal of Solid State Chemistry* **268**, 123 (2018).
- [35] R. W. Smaha, W. He, J. M. Jiang, J. Wen, Y.-F. Jiang, J. P. Sheckelton, C. J. Titus, S. G. Wang, Y.-S. Chen, S. J. Teat, *et al.*, Materializing rival ground states in the barlowite family of kagome magnets: quantum spin liquid, spin ordered, and valence bond crystal states, *npj Quantum Materials* **5**, 1 (2020).
- [36] A. Henderson, L. Dong, S. Biswas, H. I. Revell, Y. Xin, R. Valenti, J. A. Schlueter, and T. Siegrist, Order-disorder transition in the $s = 1/2$ kagome antiferromagnets claringbullite and barlowite, *Chem. Commun.* **55**, 11587 (2019).
- [37] K. Tustain, B. Ward-O'Brien, F. Bert, T. H. Han, H. Luetkens, T. Lancaster, B. M. Huddart, P. J. Baker, and L. Clark, From magnetic order to quantum disorder: a μSR study of the Zn-barlowite series of $S = \frac{1}{2}$ kagomé antiferromagnets, $\text{Zn}_x\text{Cu}_{4-x}(\text{OH})_6\text{FBr}$ (2020), [arXiv:2005.12615 \[cond-mat.str-el\]](https://arxiv.org/abs/2005.12615).
- [38] Y. Wei, X. Ma, Z. Feng, D. Adroja, A. Hillier, P. Biswas, A. Senyshyn, C.-W. Wang, A. Hoser, J.-W. Mei, Z. Y. Meng, H. Luo, Y. Shi, and S. Li, Magnetic phase diagram of $\text{Cu}_{4-x}\text{Zn}_x(\text{OH})_6\text{FBr}$ studied by neutron-diffraction and μSR techniques (2020), [arXiv:2007.11816 \[cond-mat.str-el\]](https://arxiv.org/abs/2007.11816).
- [39] W.-H. Ko, Z.-X. Liu, T.-K. Ng, and P. A. Lee, Raman signature of the U(1) Dirac spin-liquid state in the spin- $\frac{1}{2}$ kagome system, *Phys. Rev. B* **81**, 024414 (2010).
- [40] P. Puphal, K. M. Zoch, J. Désor, M. Bolte, and C. Krellner, Kagome quantum spin systems in the atacamite family, *Phys. Rev. Materials* **2**, 063402 (2018).
- [41] A. Zorko, M. Pregelj, M. Gomilšek, M. Klanjšek, O. Zaharko, W. Sun, and J.-X. Mi, Negative-vector-chirality 120° spin structure in the defect- and distortion-free quantum kagome antiferromagnet $\text{YCu}_3(\text{OH})_6\text{Cl}_3$, *Phys. Rev. B* **100**, 144420 (2019).
- [42] T. Arh, M. Gomilšek, P. Prelovšek, M. Pregelj, M. Klanjšek, A. Ozarowski, S. J. Clark, T. Lancaster, W. Sun, J.-X. Mi, and A. Zorko, Origin of magnetic ordering in a structurally perfect quantum kagome antiferromagnet, *Phys. Rev. Lett.* **125**, 027203 (2020).
- [43] D. E. Freedman, T. H. Han, A. Prodi, P. Müller, Q.-Z. Huang, Y.-S. Chen, S. M. Webb, Y. S. Lee, T. M. McQueen, and D. G. Nocera, Site Specific X-ray Anomalous Dispersion of the Geometrically Frustrated Kagomé Magnet, Herbertsmithite, $\text{ZnCu}_3(\text{OH})_6\text{Cl}_2$, *J. Am. Chem. Soc.* **132**, 16185 (2010).
- [44] O. Cépas, J. O. Haerter, and C. Lhuillier, Detection of weak emergent broken-symmetries of the kagome antiferromagnet by raman spectroscopy, *Phys. Rev. B* **77**, 172406 (2008).
- [45] X.-L. Liu, X. Zhang, M.-L. Lin, and P.-H. Tan, Different angle-resolved polarization configurations of raman spectroscopy: A case on the basal and edge plane of two-dimensional materials, *Chinese Physics B* **26**, 067802 (2017).
- [46] J. W. Halley, Light scattering as a probe of dynamical critical properties of antiferromagnets, *Phys. Rev. Lett.* **41**, 1605 (1978).
- [47] G. F. Reiter, Light scattering from energy fluctuations in magnetic insulators, *Phys. Rev. B* **13**, 169 (1976).
- [48] P. Lemmens, G. Güntherodt, and C. Gros, Magnetic light scattering in low-dimensional quantum spin systems, *Physics Reports* **375**, 1 (2003).
- [49] T. P. Devereaux and R. Hackl, Inelastic light scattering from correlated electrons, *Rev. Mod. Phys.* **79**, 175 (2007).
- [50] P. A. Fleury and R. Loudon, Scattering of light by one- and two-magnon excitations, *Phys. Rev.* **166**, 514 (1968).
- [51] B. S. Shastry and B. I. Shraiman, Theory of Raman scattering in Mott-Hubbard systems, *Phys. Rev. Lett.* **65**, 1068 (1990).
- [52] P. A. Lee, N. Nagaosa, and X.-G. Wen, Doping a Mott insulator: Physics of high-temperature superconductivity, *Rev. Mod. Phys.* **78**, 17 (2006).
- [53] B. Bernu, L. Pierre, K. Essafi, and L. Messio, Effect of perturbations on the kagome $s = \frac{1}{2}$ antiferromagnet at all temperatures, *Phys. Rev. B* **101**, 140403 (2020).
- [54] W. Sun, Y.-X. Huang, S. Nokhrin, Y. Pan, and J.-X. Mi, Perfect Kagomé lattices in $\text{YCu}_3(\text{OH})_6\text{Cl}_3$: a new candidate for the quantum spin liquid state, *J. Mater. Chem. C* **4**, 8772 (2016).
- [55] R. Okuma, T. Yajima, D. Nishio-Hamane, T. Okubo, and Z. Hiroi, Weak ferromagnetic order breaking the threefold rotational symmetry of the underlying kagome lattice in $\text{CdCu}_3(\text{OH})_6(\text{NO}_3)_2 \cdot \text{H}_2\text{O}$, *Phys. Rev. B* **95**, 094427 (2017).
- [56] K. Iida, H. K. Yoshida, A. Nakao, H. O. Jeschke, Y. Iqbal, K. Nakajima, S. Ohira-Kawamura, K. Munakata, Y. Inamura,

- N. Murai, M. Ishikado, R. Kumai, T. Okada, M. Oda, K. Kakurai, and M. Matsuda, $q = 0$ long-range magnetic order in centennialite $\text{CaCu}_3(\text{OD})_6\text{Cl}_2 \cdot 0.6\text{D}_2\text{O}$: A spin- $\frac{1}{2}$ perfect kagome antiferromagnet with $J_1 - J_2 - J_d$, *Phys. Rev. B* **101**, 220408 (2020).
- [57] S. Chu, P. Müller, D. G. Nocera, and Y. S. Lee, Hydrothermal growth of single crystals of the quantum magnets: Clinoatacamite, paratacamite, and herbertsmithite, *Applied Physics Letters* **98**, 092508 (2011).
- [58] M. Velázquez, F. Bert, P. Mendels, D. Denux, P. Veber, M. Lahaie, and C. Labrugère, Aqueous solution growth at 200°C and characterizations of pure, ^{17}O - or $^{\text{D}}$ -based herbertsmithite $\text{Zn}_x\text{Cu}_{4-x}(\text{OH})_6\text{Cl}_2$ single crystals, *Journal of Crystal Growth* **531**, 125372 (2020).
- [59] O. V. Dolomanov, L. J. Bourhis, R. J. Gildea, J. A. Howard, and H. Puschmann, Olex2: a complete structure solution, refinement and analysis program, *Journal of applied crystallography* **42**, 339 (2009).
- [60] O. Cépas, C. M. Fong, P. W. Leung, and C. Lhuillier, Quantum phase transition induced by dzyaloshinskii-moriya interactions in the kagome antiferromagnet, *Phys. Rev. B* **78**, 140405 (2008).
- [61] I. Rousochatzakis, S. R. Manmana, A. M. Läuchli, B. Normand, and F. Mila, Dzyaloshinskii-Moriya anisotropy and nonmagnetic impurities in the $s = \frac{1}{2}$ kagome system $\text{ZnCu}_3(\text{OH})_6\text{Cl}_2$, *Phys. Rev. B* **79**, 214415 (2009).
- [62] W. Zhu, S.-s. Gong, and D. N. Sheng, Identifying spinon excitations from dynamic structure factor of spin-1/2 heisenberg antiferromagnet on the kagome lattice, *Proceedings of the National Academy of Sciences* **116**, 5437 (2019).
- [63] A. L. Chernyshev and M. E. Zhitomirsky, Quantum Selection of Order in an XXZ Antiferromagnet on a Kagome Lattice, *Phys. Rev. Lett.* **113**, 237202 (2014).

METHODS

Sample preparation and characterization. High qualified single crystals of Zn-Barlowite was grown by a hydrothermal method similar to crystal growth of herbertsmithite.[57, 58] CuO (0.6 g), ZnBr_2 (3 g), and NH_4F (0.5 g) and 18 ml deionized water were sealed in a quartz tube and heated between 200 °C and 140 °C by a two-zone furnace. After three months, we obtained millimeter-sized single crystal samples. The value of x in $\text{Cu}_{4-x}\text{Zn}_x(\text{OH})_6\text{FBr}$ has been determined as 0.82 by Inductively Coupled Plasma-Atomic Emission Spectroscopy (ICP-AES). The single-crystal X-ray diffraction has been carried out at room temperature by using Cu source radiation ($\lambda = 1.54178 \text{ \AA}$) and solved by the Olex2.PC suite programs.[59] The structure and cell parameters of $\text{Cu}_{4-x}\text{Zn}_x(\text{OH})_6\text{FBr}$ are in coincidence with the previous report on polycrystalline samples.[30, 32] For Barlowite($\text{Cu}_4(\text{OH})_6\text{FBr}$), the mixture of CuO (0.6 g), MgBr_2 (1.2 g), and NH_4F (0.5 g) was transferred into Teflon-lined autoclave with 10 ml water. The autoclave was heated up to 260 °C and cooled to 140 °C after two weeks. A similar growth condition to Barlowite was applied for the growth of $\text{EuCu}_3(\text{OH})_6\text{Cl}_3$ with starting materials of $\text{EuCl}_3 \cdot 6 \text{H}_2\text{O}$ (2 g) and CuO (0.6 g).

Measurement methods. Our thermodynamical measure-

ments were carried out on the Physical Properties Measurement System (PPMS, Quantum Design) and the Magnetic Property Measurement System (MPMS3, Quantum Design).

The temperature-dependent Raman spectra are measured in a backscattering geometry using a home-modified Jobin-Yvon HR800 Raman system equipped with an electron-multiplying charged-coupled detector (CCD) and a $50\times$ objective with long working distance and numerical aperture of 0.45. The laser excitation wavelength is 514 nm from an Ar^+ laser. The laser-plasma lines are removed using a BragGrate bandpass filter (OptiGrate Corp.), while the Rayleigh line is suppressed using three BragGrate notch filters (BNFs) with an optical density 4 and a spectral bandwidth $\sim 5\text{-}10 \text{ cm}^{-1}$. The 1800 lines/mm grating enables each CCD pixel to cover 0.6 cm^{-1} . The samples are cooled down to 30 K using a Montana cryostat system under a vacuum of 0.4 mTorr and down to 4 K using an attoDRY 1000 cryogenic system. All the measurements are performed with a laser power below 1 mW to avoid sample heating. The temperature is calibrated by the Stocks-anti-Stocks relation for the magnetic Raman continuum and phonon peaks. The intensities in two cryostat systems are matched by the Raman susceptibility. The polarized Raman measurements with light polarized in the ab kagome plane of samples were performed in parallel (XX), perpendicular (XY), and X -only polarization configurations [Supplementary Section4].

SHG measurements were performed using a homemade confocal microscope in a back-scattering geometry. A fundamental wave centered at 800 nm was used as excitation source, which was generated from a Ti-sapphire oscillator (Chameleon Ultra II) with an 80 MHz repetition frequency and a 150 fs pulse width. After passing through a $50\times$ objective, the pump beam was focused on the sample with a diameter of $2 \mu\text{m}$. The scattering SHG signals at 400 nm were collected by the same objective and led to the entrance slit of a spectrometer equipped with a thermoelectrically cooled CCD. Two shortpass filters were employed to cut the fundamental wave.

Magnon peak in Raman response for $q = 0$ AFM state.

We consider a kagome lattice antiferromagnet with the DM interaction

$$H = J \sum_{\langle ij \rangle} (\mathbf{S}_i \cdot \mathbf{S}_j) + D \hat{z} \cdot \sum_{\langle ij \rangle} \mathbf{S}_i \times \mathbf{S}_j, \quad (2)$$

where summation runs over nearest neighbor bonds $\langle ij \rangle$ of the kagome lattice, and the DM interaction is assumed to be of the out-of-plane type. With a large DM interaction D , the kagome antiferromagnet devoleps a $\mathbf{q} = 0$ type 120° AFM order at low temperature in EuCu_3 . [40–42, 60–62] In terms of the local basis for the AFM order, we rewrite the Hamiltonian as

$$H = J \sum_{\langle ij \rangle} \mathbf{S}_i \odot \mathbf{S}_j + D \sum_{\langle ij \rangle} \mathbf{S}_i \otimes \mathbf{S}_j, \quad (3)$$

with

$$\begin{aligned}\mathbf{S}_i \odot \mathbf{S}_j &= S_i^x S_j^x + \cos(\theta_{ij})(S_i^y S_j^y + S_i^z S_j^z) \\ &\quad + \sin(\theta_{ij})(S_i^z S_j^y - S_i^y S_j^z), \\ \mathbf{S}_i \otimes \mathbf{S}_j &= \sin(\theta_{ij})(S_i^y S_j^y + S_i^z S_j^z) \\ &\quad + \cos(\theta_{ij})(S_i^y S_j^z - S_i^z S_j^y),\end{aligned}\quad (4)$$

where θ_{ij} is an angle between two neighboring spins. The effective linear spin wave Hamiltonian is given as

$$\mathcal{H}_{\text{eff}} = J \sum_{\langle ij \rangle} [S_i^x S_j^x + (\cos \theta_{ij} + \sin \theta_{ij} D/J) \times (S_i^y S_j^y + S_i^z S_j^z)],\quad (5)$$

for which the Holstein-Primakoff representation for spin operators in the local basis was applied and the energy dispersion was obtained in Ref. [63].

The Raman tensor in the XY configuration is given as

$$\begin{aligned}\tau_R^{xy} &= \sum_{\langle ij \rangle} \mathbf{r}_{ij}^x \mathbf{r}_{ij}^y \mathbf{S}_i \cdot \mathbf{S}_j, \\ &= \frac{\sqrt{3}}{4} \sum_R \mathbf{S}_{R3} \cdot (\mathbf{S}_{R1} + \mathbf{S}_{R+\mathbf{a}_2} - \mathbf{S}_2 - \mathbf{S}_{R-\mathbf{a}_1+\mathbf{a}_2}).\end{aligned}\quad (6)$$

In the local spin basis, we have the Raman tensor is given as

$$\begin{aligned}\tau_R^{xy} &= \frac{\sqrt{3}}{4} \sum_R \mathbf{S}_{R3} \odot (\mathbf{S}_{R1} + \mathbf{S}_{R+\mathbf{a}_2} - \mathbf{S}_2 \\ &\quad - \mathbf{S}_{R-\mathbf{a}_1+\mathbf{a}_2}).\end{aligned}\quad (7)$$

In the spin-pair operator $\mathbf{S}_i \odot \mathbf{S}_j$ in Eq. (4), there are two-magnon contribution in terms of $S_i^x S_j^x + \cos(\theta_{ij})(S_i^y S_j^y + S_i^z S_j^z)$, and one- and three-magnon contributions in terms of $\sin(\theta_{ij})(S_i^z S_j^y - S_i^y S_j^z)$. For the $\mathbf{q} = 0$ spin configuration, we find that τ_R^{xy} in Eq. 7 has the non-vanished one magnon contributions. For the $\sqrt{3} \times \sqrt{3}$ AFM state, τ_R^{xy} has no one-magnon contribution. The observed one-magnon peak in the E_g channel in EuCu_3 provides evidence for the $\mathbf{q} = 0$ spin ordering at low temperatures. In the linear spin-wave theory,

we take S^z in the local basis as a constant, $S_i^z = \langle S^z \rangle = 1/2$, and the XY Raman tensor is given as

$$\tau_R^{xy} = \frac{3}{8} \sum_R (S_{R1}^y + S_{R2}^y - 2S_{R3}^y),\quad (8)$$

in terms of the local basis, directly measuring the one magnon excitation. For EuCu_3 , we have the estimation for the interaction parameters, $J = 10$ meV, $D/J = 0.3$, and the magnon peak position is $\Delta_{sw} = 1.1J = 88$ cm^{-1} , very close to the measured value 72 cm^{-1} in our Raman measurement of the one-magnon peak.

Data Availability All data supporting the findings of this study are available from the corresponding authors upon reasonable request.

Acknowledgments: This work was supported by the National Key Research and Development Program of China (2016YFA0301204), the program for Guangdong Introducing Innovative and Entrepreneurial Teams (No. 2017ZT07C062), by Shenzhen Key Laboratory of Advanced Quantum Functional Materials and Devices (No. ZDSYS20190902092905285), and by National Natural Science Foundation of China (Grant No.11774143, 12004377 and 11874350), the CAS Key Research Program of Frontier Sciences (ZDBS-LYSLH004) and China Postdoctoral Science Foundation (2019TQ0317). P.A. Lee acknowledges support by the US Department of Energy under grant number DE-FG02-03ER46076.

Competing Interests: The Authors declare no competing financial or non-financial interests.

Author Contributions: J.W.Mei conceived the project. P.H.Tan directed the experimental work of Raman. Y.Fu, L.Wang, L.Huang, W.Jiang and Z.Hao synthesized single crystals of samples. M.Lin and P.H.Tan designed the Raman experiments. M.Lin, P.H.Tan and J.Zhang performed Raman measurements. Q.Liu and J.Dai performed the SHG measurements. Y.Fu, L.Wang, L.Huang and C.Liu performed and analyzed magnetic susceptibility and heat capacity measurements. H.Zhang, X.Shi and J.W.Mei performed first-principles calculations. J.W.Mei, Y.Fu, M.Lin and P.H.Tan analyzed the Raman data. P.A.Lee, J.W.Mei and F.Ye worked on the theory, and wrote the manuscript with contributions and comments from all authors.

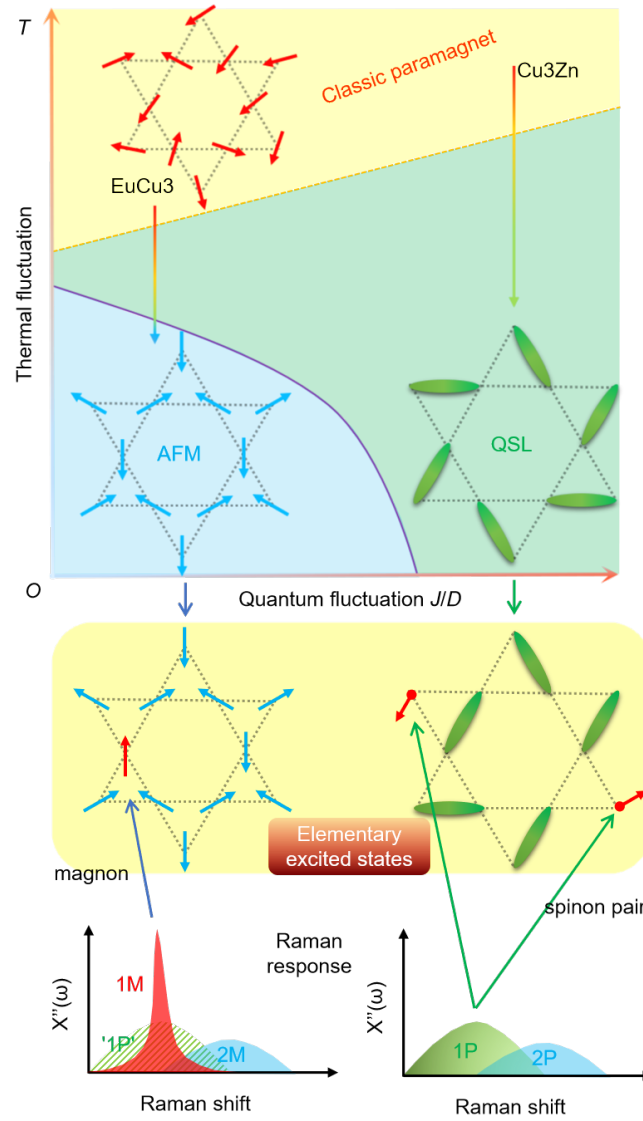


FIG. 1. **Schematic comparative Raman responses for the AFM and QSL states.** With a large DM interaction D , the kagome antiferromagnet develops a 120° non-collinear AFM ground state with the wave vector $\mathbf{q} = 0$ below T_N . [60–62] Increasing J/D , the fluctuation of the kagome system increases, driving the system into the QSL state. By increasing the temperature, the thermal fluctuation melts the magnetic order and turns the system into the classic paramagnetic state at high temperatures. By the first-principle calculations in Supplementary Section 8, Cu_3Zn and EuCu_3 have the values of D/J as 0.05 and 0.3, and thus correspond to the QSL and AFM ground states, respectively. In the middle, the elementary excited states of AFM and QSL states are the magnon and spinon, respectively, resulting in different magnetic Raman spectra shown at the bottom. Here 1P and 2P denote the one-pair and two-pair spinon excitations, respectively. 1M and 2M in magnetically ordered state denote the one- and two-magnon excitations, respectively. The 1M Raman peak in AFM measures the magnon [Methods Section] while the 1P Raman continuum in QSL probes the spinon excitations. [39] The shadow background of the 1M peak, marked as ‘1P’, denotes the continuum above T_N in EuCu_3 , mimicking the 1P continuum in the QSL state [Supplementary Section 6]. So the magnon excitation below T_N emerges from the one-pair continuum and can be regarded as the bound state of the spinon-antispinon excitations. The transition between QSL and AFM can be thought to be driven by the spinon confinement.

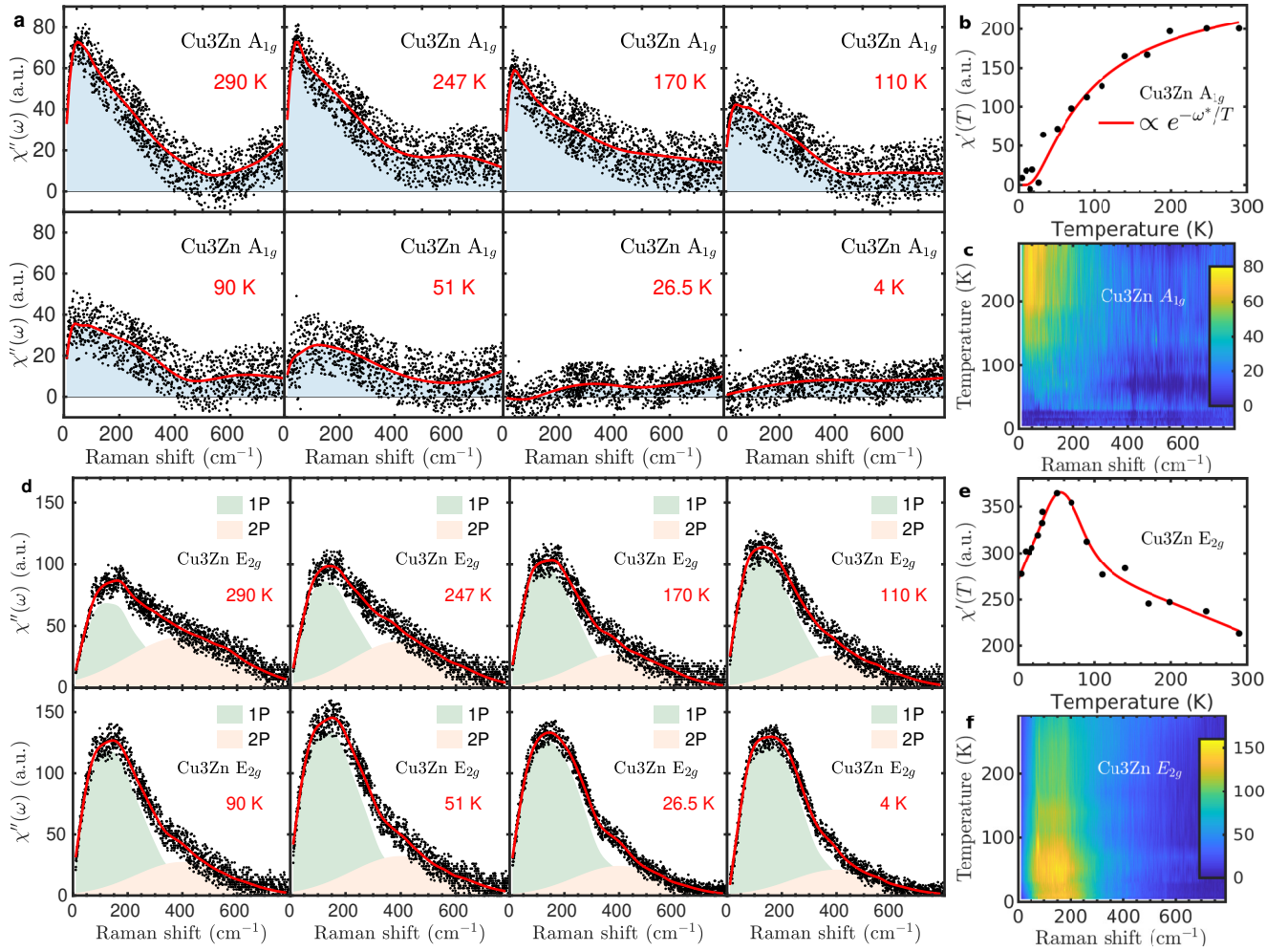


FIG. 2. Temperature dependence of the Raman susceptibilities in Cu3Zn. (a) The A_{1g} Raman susceptibility $\chi''_{A_{1g}} = \chi''_{XX} - \chi''_{YY}$. The solid lines are a guide to the eye. (b) Temperature dependence of the static Raman susceptibility in A_{1g} channel $\chi'_{A_{1g}}(T) = \frac{2}{\pi} \int_{10}^{400} \text{cm}^{-1} \frac{\chi''_{A_{1g}}(\omega)}{\omega} d\omega$. The solid line is a thermally activated function. (c) Color map of the temperature dependence of the magnetic Raman continuum $\chi'_{A_{1g}}(\omega, T)$. (d) The E_{2g} Raman response function $\chi''_{E_{2g}} = \chi''_{XY}$. The solid lines are a guide to the eye. We schematically decompose the E_{2g} magnetic Raman continuum into two components of spin excitations for one and two spin-antispinon pair excitations, respectively. Here 1P and 2P represent one- and two-pair, respectively. (e) Temperature dependence of the static Raman susceptibility in E_{2g} channel $\chi'_{E_{2g}} = \frac{2}{\pi} \int_{10}^{780} \text{cm}^{-1} \frac{\chi''_{E_{2g}}(\omega)}{\omega} d\omega$. The solid line is a guide to the eye. (f) Color map of the temperature dependence of the magnetic Raman continuum $\chi'_{E_{2g}}(\omega, T)$.

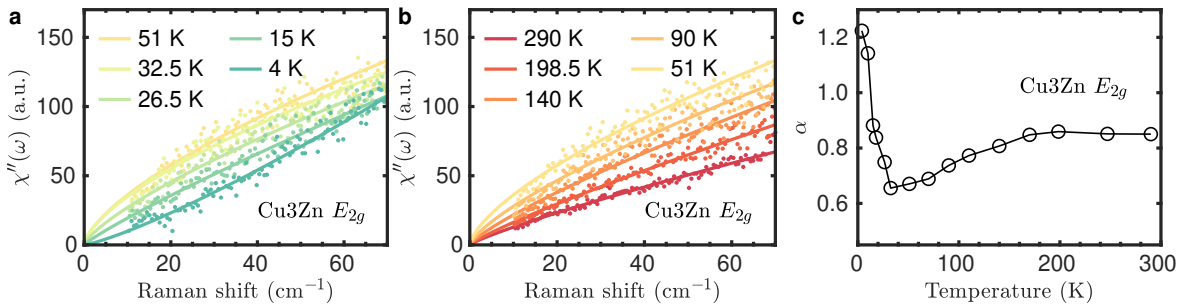


FIG. 3. Power-law behavior for the E_{2g} Raman continua at low frequency in Cu3Zn. (a) and (b) Power-law fitting of $\chi''_{E_{2g}}(\omega) \propto \omega^\alpha$ at low and high temperatures, respectively, in Cu3Zn. (c) Temperature dependent exponent α for the power-law fittings in Cu3Zn.

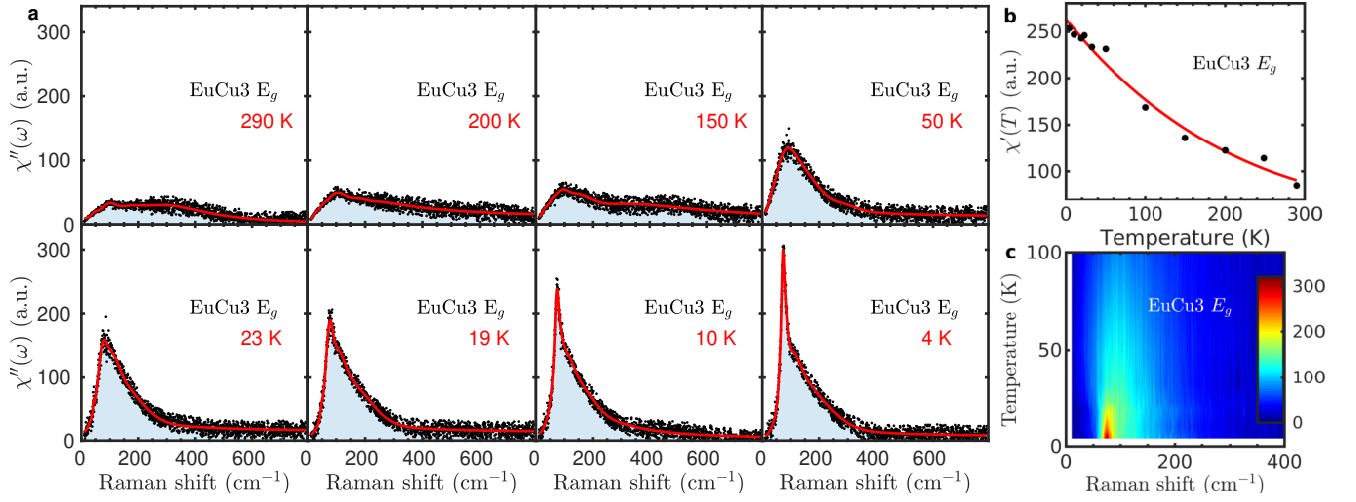


FIG. 4. **temperature dependence of the e_g Raman susceptibilities in eucu3.** (a) the e_g Raman susceptibility $\chi''_{e_g} = \chi''_{xy}$. the solid lines are a guide to the eye. a sharp magnon peak appears in the e_g magnetic Raman continuum below the magnetic transition temperature $t_n = 17$ k. (b) temperature dependence of the static Raman susceptibility in e_g channel $\chi'_{e_g} = \frac{2}{\pi} \int_{10}^{780 \text{ cm}^{-1}} \frac{\chi''_{e_g}(\omega)}{\omega} d\omega$. the solid line is a guide to the eye. (c) Color map of the temperature dependence of the magnetic Raman continuum $\chi''_{E_g}(\omega, T)$. A sharp magnon peak is observed below T_N .

Supplementary Information: Dynamic fingerprint of fractionalized excitations in single-crystalline $\text{Cu}_3\text{Zn}(\text{OH})_6\text{FBr}$

Ying Fu,^{1,*} Miao-Ling Lin,^{2,3,*} Le Wang,¹ Qiye Liu,¹ Lianglong Huang,¹ Wenrui Jiang,¹ Zhanyang Hao,¹ Cai Liu,¹ Hu Zhang,⁴ Xingqiang Shi,⁴ Jun Zhang,^{2,3} Junfeng Dai,¹ Dapeng Yu,¹ Fei Ye,^{1,5} Patrick A. Lee,⁶ Ping-Heng Tan,^{2,3,†} and Jia-Wei Mei^{1,5,‡}

¹*Shenzhen Institute for Quantum Science and Engineering, and Department of Physics, Southern University of Science and Technology, Shenzhen 518055, China*

²*State Key Laboratory of Superlattices and Microstructures, Institute of Semiconductors, Chinese Academy of Sciences, Beijing 100083, China*

³*Center of Materials Science and Optoelectronics Engineering & CAS Center of Excellence in Topological Quantum Computation, University of Chinese Academy of Sciences, 100049 Beijing, China*

⁴*College of Physics Science and Technology, Hebei University, Baoding 071002, China*

⁵*Shenzhen Key Laboratory of Advanced Quantum Functional Materials and Devices, Southern University of Science and Technology, Shenzhen 518055, China*

⁶*Department of Physics, Massachusetts Institute of Technology, Cambridge, Massachusetts 02139, USA*
(Dated: October 16, 2020)

CONTENTS

I. Crystal photograph and thermodynamic characterization	2
II. Temperature evolution of the Raman spectra and phonon mode assignment in Cu_3Zn	3
III. Raman spectra evolution from Cu_4 to Cu_3Zn and Fano effect in Cu_3Zn	4
IV. Angle-resolved light polarization dependent Raman response for Cu_3Zn	5
V. Raman responses in EuCu_3	6
VI. Magnetic continuum in EuCu_3 above T_N	7
VII. SHG of Cu_3Zn	8
VIII. Estimation of exchange parameters in the kagome compounds	9
References	9

* These two authors contributed equally.

† phtan@semi.ac.cn

‡ meijw@sustech.edu.cn

I. CRYSTAL PHOTOGRAPH AND THERMODYNAMIC CHARACTERIZATION

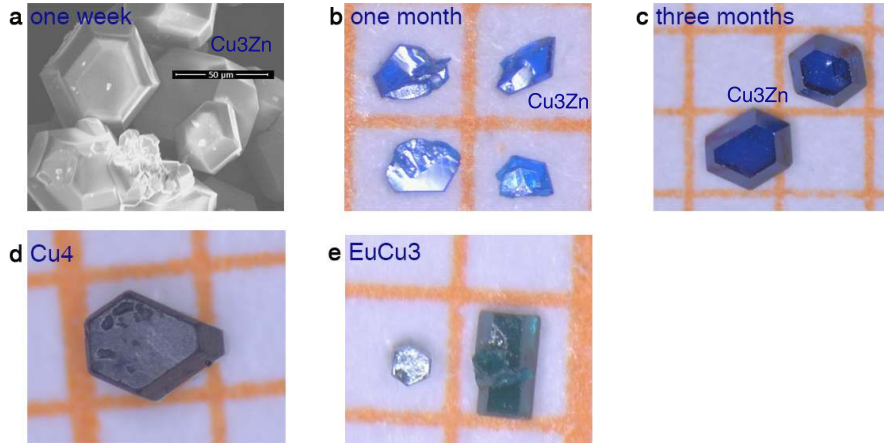


FIG. S1. **Photographs for single crystals of Cu_3Zn , Cu_4 and EuCu_3 .** Crystal sizes and morphologies of $\text{Cu}_3\text{Zn}(\text{OH})_6\text{FBr}$ (Cu_3Zn) for different growth periods: (a) one week, (b) one month, and (c) three months. (d) $\text{Cu}_4(\text{OH})_6\text{FBr}$ (Cu_4); (e) $\text{EuCu}_3(\text{OH})_6\text{Cl}_3$ (EuCu_3). The yellow grid in (b), (c), (d) and (e) is $1 \times 1 \text{ mm}^2$.

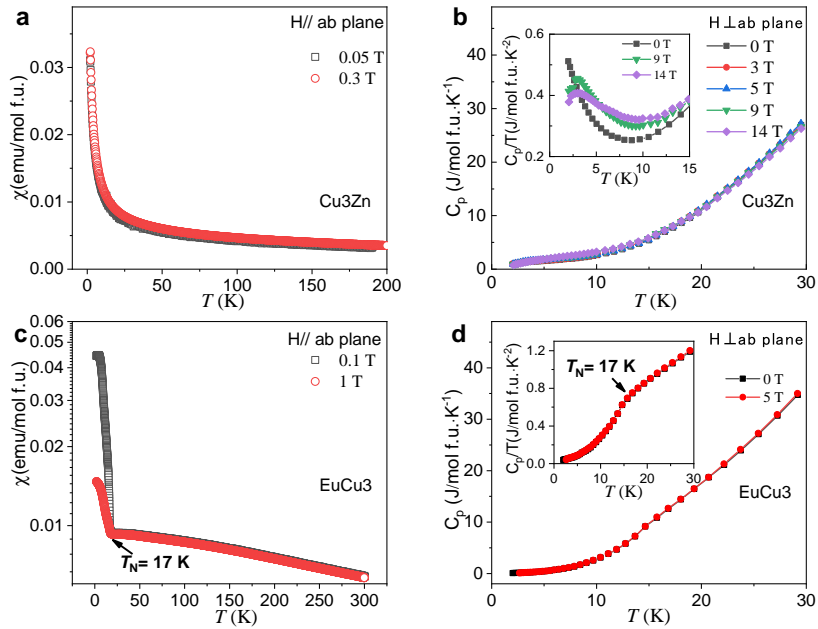


FIG. S2. **Thermodynamic properties of single crystals for Cu_3Zn and EuCu_3 .** (a) Temperature dependent magnetic susceptibilities ($\chi = M/H$) at 0.05 T and 0.3 T fields. (b) The temperature dependent specific heat C_p at different magnetic fields in Cu_3Zn . The thermodynamic properties of single crystals for Cu_3Zn agree well with previous results on the powder samples.[1, 2] (c) The magnetic susceptibilities show the ordering temperature $T_N = 17 \text{ K}$ in EuCu_3 . The Eu^{3+} with ground state of 7F_0 contributes to the Van Vleck paramagnetism (d) The temperature dependent heat capacities C_p in EuCu_3 .

II. TEMPERATURE EVOLUTION OF THE RAMAN SPECTRA AND PHONON MODE ASSIGNMENT IN Cu₃Zn

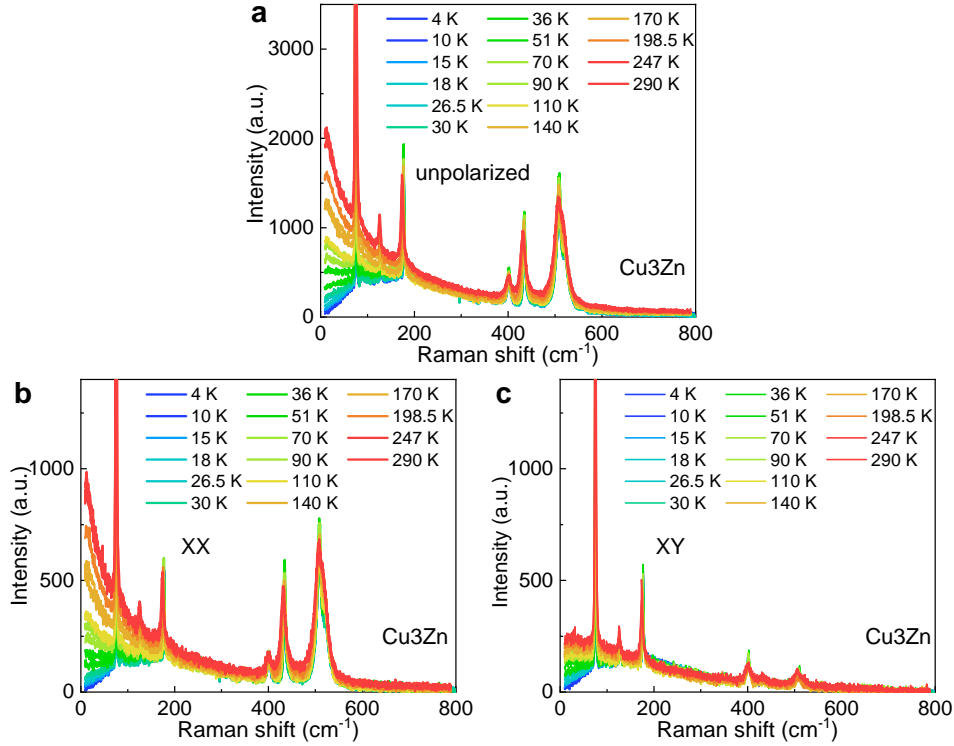


FIG. S3. **Raman spectra in Cu₃Zn at different temperatures.** (a) Unpolarized Raman spectra in Cu₃Zn. (b) Raman spectra in the *XX* configuration in Cu₃Zn which contains the A_{1g} and E_{2g} channel. (c) Raman spectra in the *XY* configuration which contains the E_{2g} channel in Cu₃Zn.

TABLE S1. Mode assignment for Cu₃Zn. Cu₃Zn crystallizes the space group $P6_3/mmc$ (No. 194) and has Raman active A_{1g} , E_{1g} , and E_{2g} modes according to the point group representation of D_{6h} ($6/mmm$). E_{1g} is not visible when the light polarization lies in the kagome ab plane, and we have Raman active phonon modes $\Gamma_{\text{Raman}} = 4A_{1g} + 9E_{2g}$.

Frequency (Exp.) (cm ⁻¹)	Modes (Exp.)	Frequency (Cal.) (cm ⁻¹)	Modes (Cal.)	Associated vibrating ions
74.6	E_{2g}	71.2	E_{2g}	Br ⁻
126.4	E_{2g}	124.11	E_{2g}	Zn ²⁺
172.2	E_{2g}	184.18	E_{2g}	F ⁻
355.5	E_{2g}	345.37	E_{2g}	O ²⁻
401.5	E_{2g}	396.21	E_{2g}	O ²⁻
430.8	A_{1g}	426.06	A_{1g}	O ²⁻
488.6	E_{2g} , visible in 532 nm	493.47	E_{2g}	O ²⁻
521.1	A_{1g}	508.84	A_{1g}	O ²⁻
920.3	E_{2g}	920.33	E_{2g}	H ⁺
1016.7	A_{1g}	1082.26	A_{1g}	H ⁺
1028.2	E_{2g} , weak	1020.11	E_{2g}	H ⁺
3352.3	?	3333.19	E_{2g}	H ⁺
3467.5	A_{1g}	3512.14	A_{1g}	H ⁺

III. RAMAN SPECTRA EVOLUTION FROM Cu₄ TO Cu₃Zn AND FANO EFFECT IN Cu₃Zn

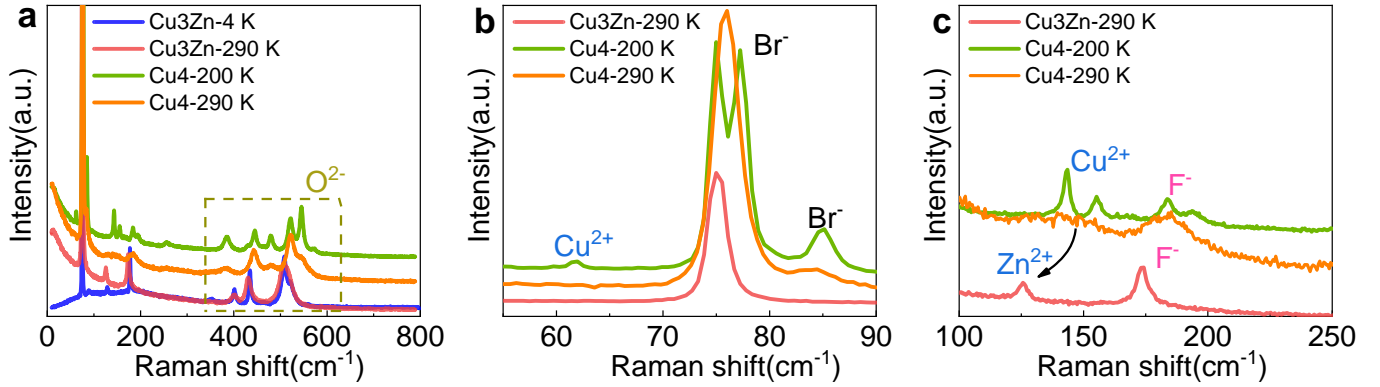


FIG. S4. **Raman spectral evolution from Cu₄ to Cu₃Zn** (a) Unpolarized Raman spectra for Cu₄ and Cu₃Zn at selected temperatures. Comparison for phonon modes between 40 cm⁻¹ and 90 cm⁻¹ in (b), and between 100 cm⁻¹ and 250 cm⁻¹ in (c) for Cu₄ and Cu₃Zn. The Cu₄ spectra in (a), (b) and (c) have been offset vertically for clarity. The phonon evolution from Cu₄ to Cu₃Zn displays the difference by substituting Cu₄ interlayer Cu²⁺ site with Zn²⁺ in Cu₃Zn. The parent Barlowite Cu₄ transforms to orthorhombic *Pnma* below $T \approx 265$ K, characterized by changes in the relative occupancies of the interlayer Cu²⁺ site. Between 300 cm⁻¹ and 600 cm⁻¹, there are several phonon peaks associated with O²⁻ vibrations in Cu₄ and Cu₃Zn. Cu₃Zn displays the Br⁻ in-plane relative mode (E_{2g}) at 75 cm⁻¹, and has no active Raman mode related to the kagome Cu²⁺ vibrations since Cu²⁺ is the inversion center. The Br⁻ phonon mode changes into two peaks in Cu₄ due to the superlattice folding in the orthorhombic *Pnma* phase at low temperature. An additional Br⁻ peak at 85 cm⁻¹ appears in Cu₄, related to the Br vibrations along the *c*-axis. The kagome layers in Cu₄ are distorted, signaled by a new phonon mode for the kagome Cu²⁺ vibration at 62 cm⁻¹. Cu₃Zn displays sharp E_{2g} modes at 125 cm⁻¹ and 173 cm⁻¹ correspond to in-plane relative movements for Zn²⁺ and F⁻, respectively. The corresponding modes (interlayer Cu²⁺ and F⁻) in Cu₄ are broad at 290 K due to the randomly distributed interlayer Cu²⁺ and split into two peaks at 200 K.

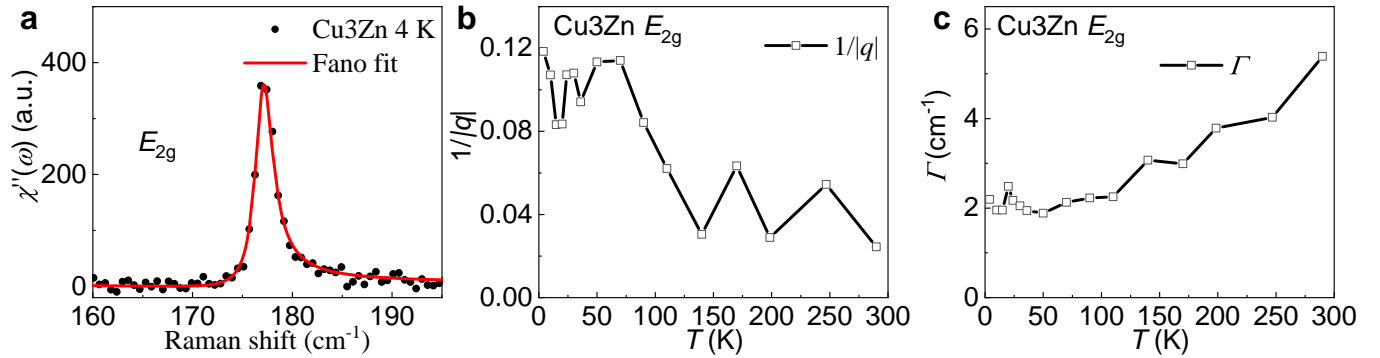


FIG. S5. **Fano lineshape of the E_{2g} F⁻ phonon peak at 173 cm⁻¹ in Cu₃Zn.** (a) Fano lineshape for the E_{2g} in-plane F atomic movement phonon mode. Temperature dependent Fano asymmetric parameter $1/|q|$ in (b) and the width Γ in (c). The asymmetric Fano lineshape provides an additional probe of the magnetic degree of freedom.

IV. ANGLE-RESOLVED LIGHT POLARIZATION DEPENDENT RAMAN RESPONSE FOR Cu₃Zn

Two typical polarization configurations were utilized to measure the angle-resolved polarized Raman spectra: i) a half-wave plate was put after the polarizer in the incident path to vary the angles between the polarization of incident laser and the analyzer with the fixed vertical polarization, which can be denoted as the X -only configuration; ii) a polarizer is allocated in the common path of the incident and scattered light to simultaneously vary their polarization directions, while the polarizations of incident laser and analyzer were parallel or perpendicular to each other. By rotating the fast axis of the half-wave plate with an angle of $\theta/2$, the polarization of incident and/or scattered light is rotated by θ .

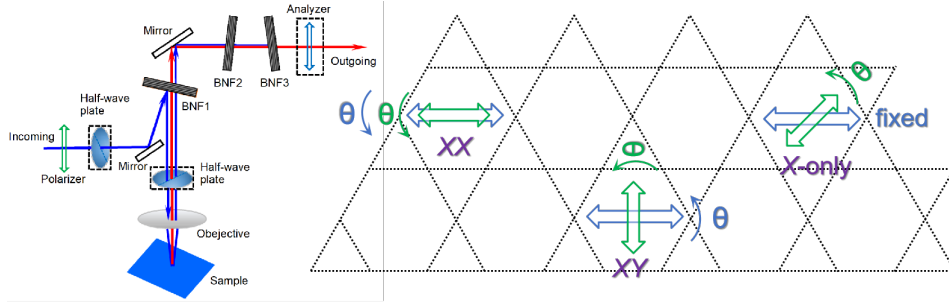


FIG. S6. **Three polarization configurations in the angle dependent Raman response.** In the XX (XY) configuration, the incoming and outgoing light polarizations are parallel (perpendicular) and we rotate both of them simultaneously. In the X -only configuration, the outgoing light polarization is fixed and we rotate the incoming light polarization only.

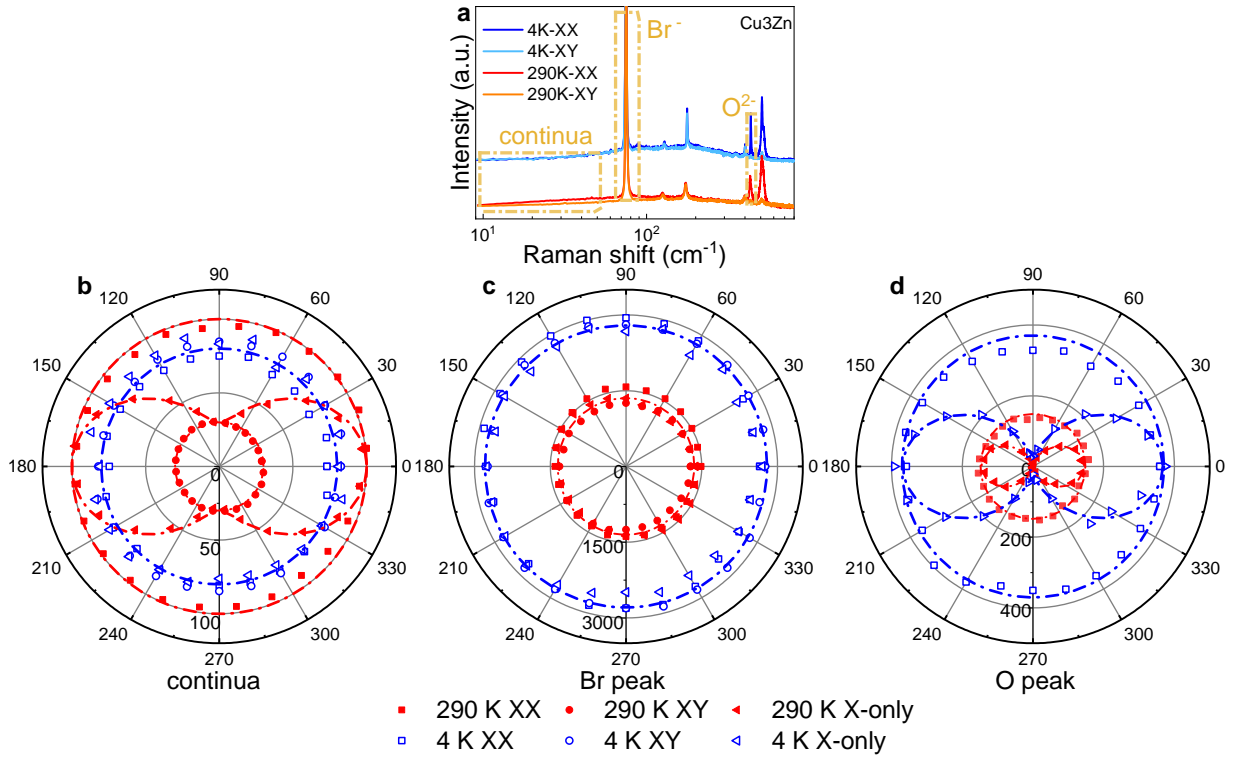


FIG. S7. **Rotation symmetry of Raman dynamics for lattice vibrations and magnetic excitations in Cu₃Zn.** (a) We monitor three selected modes (both continua and phonon peaks). (b) Angle dependence of the integrated Raman susceptibility $\chi_R = \frac{2}{\pi} \int_{10}^{60 \text{ cm}^{-1}} \frac{\chi''(\omega)}{\omega} d\omega$. In X -only configuration, the continua at 290 K follows the $\cos^2(\theta)$ for the A_{1g} channel, while at other configurations, the continua remain constant. (c) Angle dependence of the Br E_{2g} phonon (75 cm^{-1}) scattering intensity. The lines are constant functions. (d) Angle dependence of the O^{2-} A_{1g} phonon (429 cm^{-1}) scattering intensity. The Raman intensity of O^{2-} A_{1g} mode exhibits a $\cos^2(\theta)$ behavior in the X -only configuration at both room temperature and low temperature, and keeps constant in XX and XY configurations.

V. RAMAN RESPONSES IN EuCu3

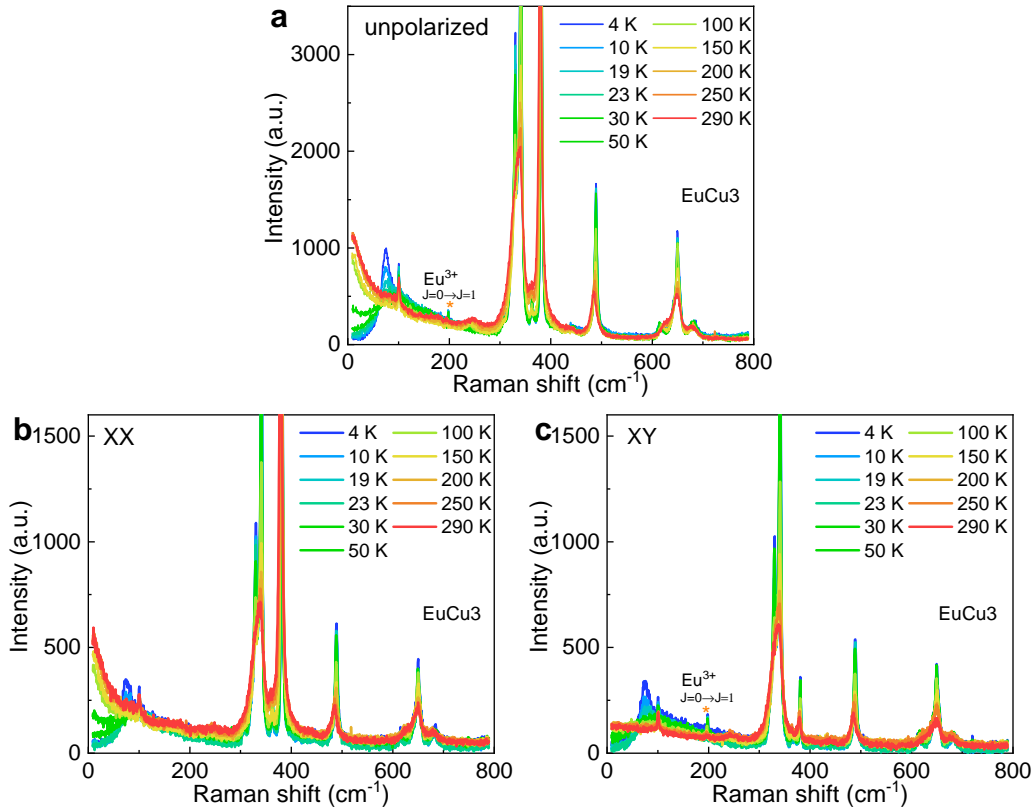


FIG. S8. **Raman spectra in EuCu3 at different temperatures.** (a) Unpolarized Raman spectra in EuCu3. (b) Raman spectra in the XX configuration in EuCu3 which has the A_g and E_g channel. (c) Raman spectra in the XY configuration which contains the E_g and A_{2g} channel. For Eu^{3+} , we observe the A_{2g} excitation of the $4f^6$ configuration with the transition from ${}^7F_{J=0}$ to ${}^7F_{J=1}$.

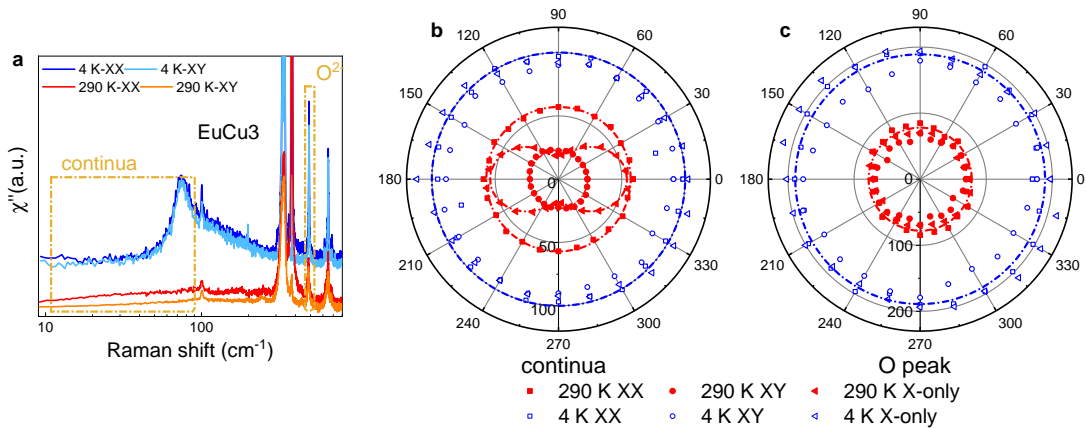


FIG. S9. **Rotation symmetry of Raman dynamics for lattice vibrations and magnetic excitations in EuCu3.** We monitor the selected magnetic continuum at low frequency and the $\text{O}^{2-} E_g$ mode in (a). (b) Angle dependence of the integrated Raman continuum from $9\text{-}80\text{ cm}^{-1}$. The continua at 290 K follows $\cos^2(\theta)$ for the A_{1g} channel, while others remain constant. (c) Angle dependence of the $\text{O}^{2-} E_g$ phonon (487 cm^{-1}) scattering intensity. Its Raman intensities are independent of θ .

VI. MAGNETIC CONTINUUM IN EuCu_3 ABOVE T_N

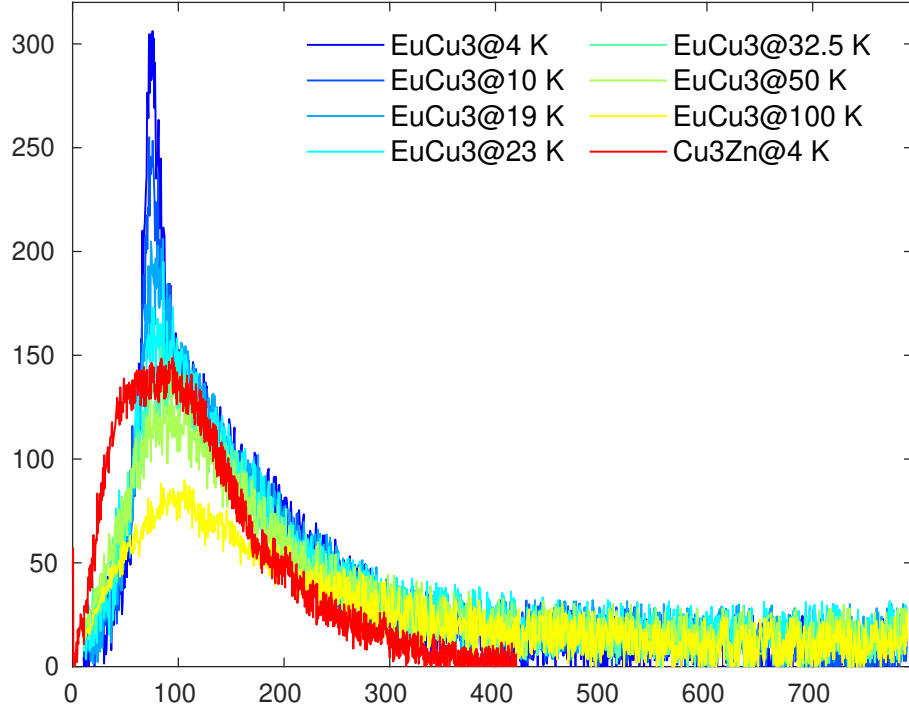


FIG. S10. **Magnetic Raman susceptibility in the XY configuration of EuCu_3 above the Néel temperature.** We present the XY magnetic Raman continuum in EuCu_3 below 100 K. Above $T_N = 17$ K, the Raman response has the substantial magnetic continuum below 50 K. For a comparison, we also plot the XY magnetic Raman continuum in Cu_3Zn at 4 K. The Raman shift frequency of Cu_3Zn is divided by 1.9, the ratio of the super-exchange strength of two compounds. We can see that above T_N , the profile of the Raman susceptibility in EuCu_3 mimic that in Cu_3Zn , suggesting the spinon contribution. There are less pronounced low-energy continuum excitations in EuCu_3 than those in Cu_3Zn , probably due to the large DM interaction which suppresses the low-energy quantum fluctuations. The maximum of the continuum excitations above T_N in EuCu_3 has the same energy scale as the magnon peak below T_N , which suggests that the magnon peak can be taken as the bound state of spinon-antispinon pair.

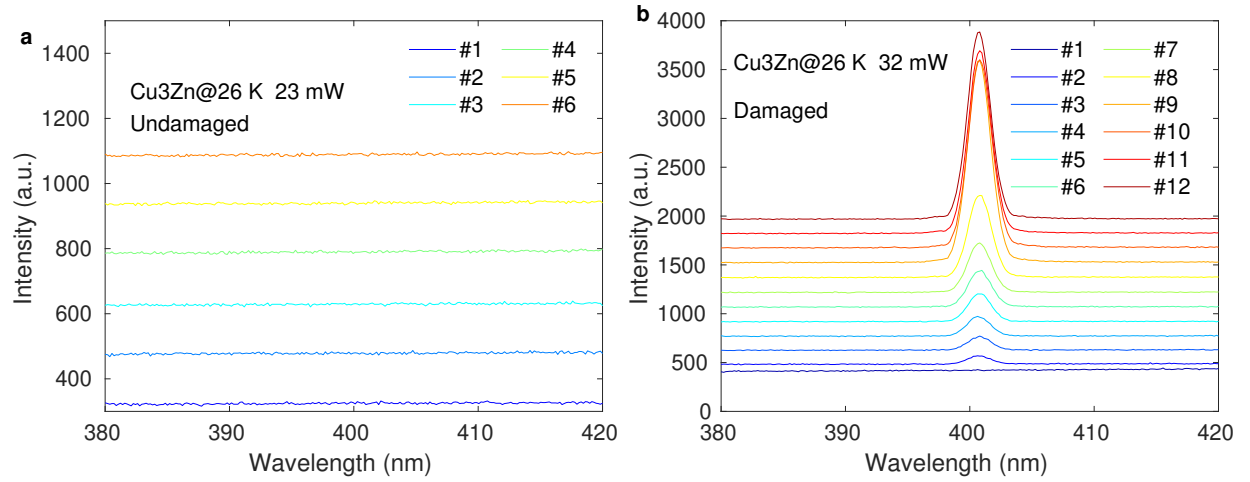
VII. SHG OF Cu₃Zn

FIG. S11. **SHG in Cu₃Zn at 26 K with different laser powers.** (a) SHG measurements in the same spot of sample taken every 5 seconds (from #1 to #6). At 23 mW, SHG signals in Cu₃Zn sample are absent, implying that inversion symmetry remains preserved. (b) A series of SHG measurements under the excitation power of 32 mW in the same point of the sample taken every 5 seconds (from #1 to #12). A remarkable SHG signal at 400 nm is detectable after a 10 second exposure, which dramatically enhances as the time increases. Due to the damage or degradation of Cu₃Zn under high power excitation, the inversion symmetry breaking induces a strong SHG signals in sample. By comparison, we conclude that undamaged Cu₃Zn single crystal presents spatial inversion symmetry at low temperature. The lines have been offset vertically for clarity.

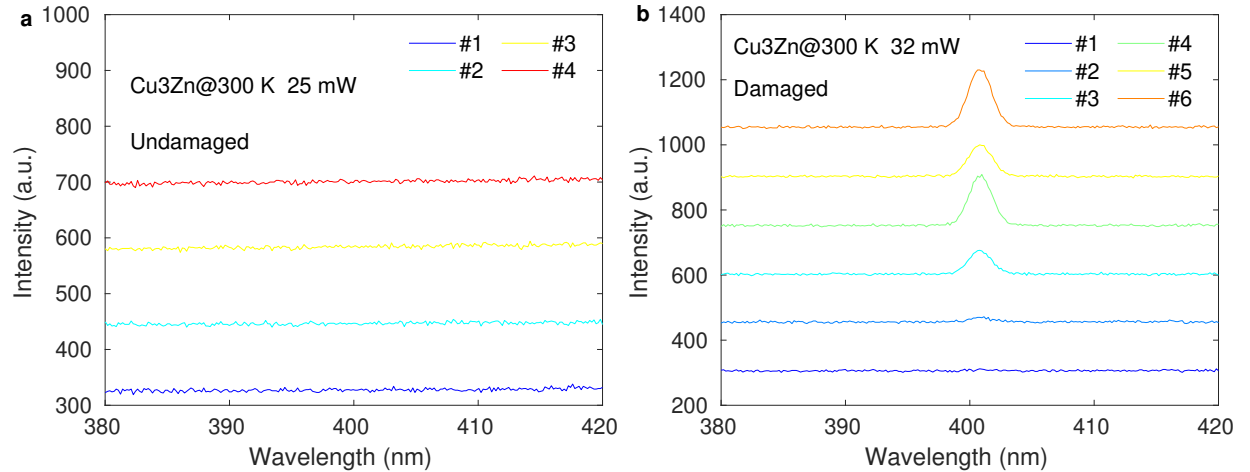


FIG. S12. **SHG in Cu₃Zn at 300 K with different laser powers.** (a) and (b) represent the successive SHG measurements in the same point of sample taken every 5 seconds with excitation powers at 25 mW and 32 mW, respectively. There are no SHG signals at the excitation power of 25 mW, whereas strong SHG signals appear at the excitation power above 32 mW after a 10 second exposure. By comparison, damage or degradation in crystal structure under high power excitation induces a detectable SHG signal, implying that inversion symmetry presents in undamaged Cu₃Zn at room temperature. The lines have been offset vertically for clarity.

VIII. ESTIMATION OF EXCHANGE PARAMETERS IN THE KAGOME COMPOUNDS

We implement the density functional theory (DFT) [3] to estimate the exchange parameters in the kagome compounds. We performed first-principles calculations with the Perdew–Burke–Ernzerhoff revised for solids (PBEsol) functional in generalized gradient approximation (GGA) [4, 5] as implemented in the Vienna Ab Initio Simulation Package (VASP).[6–8] An energy cutoff of 620 eV was used. We used $6 \times 6 \times 4$ Monkhorst-Pack grids [9] for all calculations. All results were obtained with Cu $3d$ valence electrons pseudopotential within GGA+U ($U_{3d}=6$ eV) scheme.[10]

We fix the lattice constants and relax the atomic positions with a coplanar magnetic structure with negative vector spin chirality in the presence of spin-orbit couplings in our calculations. Exchange interactions can be determined from total energies of various different spin configurations. To determine J_1 , J_2 , and J_d (see Fig. S13), we used the ferromagnetic state, antiferromagnetic state ($q = 0$), cuboc2 state, and cuboc1 state for a $2 \times 2 \times 1$ supercell as discussed in Fig. 4 in Ref. [11]. Inter-layer couplings are determined by comparing the energies for different stacking patterns of spin configurations. Note for the above interaction terms, we turn off the spin-orbit coupling in our simulations. For the Dzyaloshinski-Moriya (DM) interaction, we turn on spin-orbit couplings and compare the energies of $\mathbf{q} = 0$ antiferromagnetic states with positive and negative vector spin chiralities. The results are listed in TAB. S2. The nearest neighbor interactions in Cu₃Zn and EuCu₃ are slightly larger than the experimental values.

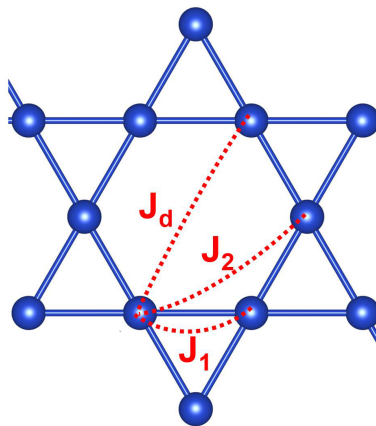


FIG. S13. Exchange interactions J_1 , J_2 , and J_d in the Kagome lattice.

TABLE S2. Theoretical results of exchange interaction (in meV) and Cu-O-Cu bonding angle for various materials with the kagome structure. SG denotes the space group. J_c denotes the inter-layer coupling. The references for the lattice constants are also listed.

Formula	SG	J_1 (meV)	J_2 (meV)	J_d (meV)	J_c (meV)	DM (meV)	\angle Cu-O-Cu ($^\circ$)	Reference
Cu ₃ Zn(OH) ₆ FBr	$P6_3/mmc$	24.13	-0.01	-0.65	1.442	1.12	117.47	[1]
YCu ₃ (OH) ₆ Cl ₃	$P\bar{3}m1$	10.21	0.12	-0.09	0.040	3.45	118.60	[12]
EuCu ₃ (OH) ₆ Cl ₃	$P\bar{3}m1$	13.02	0.16	-0.08	0.003	3.83	120.33	[13]
SmCu ₃ (OH) ₆ Cl ₃	$P\bar{3}m1$	13.55	0.14	-0.08	-0.004	5.91	120.36	[14]

- [S1] Z. Feng, Z. Li, X. Meng, W. Yi, Y. Wei, J. Zhang, Y.-C. Wang, W. Jiang, Z. Liu, S. Li, F. Liu, J. Luo, S. Li, G. qing Zheng, Z. Y. Meng, J.-W. Mei, and Y. Shi, Gapped Spin-1/2 Spinon Excitations in a New Kagome Quantum Spin Liquid Compound Cu₃Zn(OH)₆FBr, Chinese Physics Letters **34**, 077502 (2017).
- [S2] Y. Wei, Z. Feng, W. Lohstroh, C. dela Cruz, W. Yi, Z. F. Ding, J. Zhang, C. Tan, L. Shu, Y.-C. Wang, J. Luo, J.-W. Mei, Z. Y. Meng, Y. Shi, and S. Li, Evidence for a Z_2 topological ordered quantum spin liquid in a kagome-lattice antiferromagnet (2017), [arXiv:1710.02991](https://arxiv.org/abs/1710.02991).
- [S3] R. O. Jones, Density functional theory: Its origins, rise to prominence, and future, *Rev. Mod. Phys.* **87**, 897 (2015).
- [S4] J. P. Perdew, K. Burke, and M. Ernzerhof, Generalized gradient approximation made simple, *Phys. Rev. Lett.* **77**, 3865 (1996).
- [S5] J. P. Perdew, A. Ruzsinszky, G. I. Csonka, O. A. Vydrov, G. E. Scuseria, L. A. Constantin, X. Zhou, and K. Burke, Restoring the density-gradient expansion for exchange in solids and surfaces, *Phys. Rev. Lett.* **100**, 136406 (2008).

- [S6] G. Kresse and J. Furthmüller, Efficient iterative schemes for ab initio total-energy calculations using a plane-wave basis set, *Phys. Rev. B* **54**, 11169 (1996).
- [S7] M. Gajdoš, K. Hummer, G. Kresse, J. Furthmüller, and F. Bechstedt, Linear optical properties in the projector-augmented wave methodology, *Phys. Rev. B* **73**, 045112 (2006).
- [S8] J. Hafner, Ab-initio simulations of materials using vasp: Density-functional theory and beyond, *J. Comput. Chem.* **29**, 2044 (2008).
- [S9] H. J. Monkhorst and J. D. Pack, Special points for brillouin-zone integrations, *Phys. Rev. B* **13**, 5188 (1976).
- [S10] A. I. Liechtenstein, V. V. Anisimov, and J. Zaanen, Density-functional theory and strong interactions: Orbital ordering in mott-hubbard insulators, *Phys. Rev. B* **52**, R5467 (1995).
- [S11] L. Messio, C. Lhuillier, and G. Misguich, Lattice symmetries and regular magnetic orders in classical frustrated antiferromagnets, *Phys. Rev. B* **83**, 184401 (2011).
- [S12] A. Zorko, M. Pregelj, M. Gomilšek, M. Klanjšek, O. Zaharko, W. Sun, and J.-X. Mi, Negative-vector-chirality 120° spin structure in the defect- and distortion-free quantum kagome antiferromagnet $\text{YCu}_3(\text{OH})_6\text{Cl}_3$, *Phys. Rev. B* **100**, 144420 (2019).
- [S13] P. Puphal, K. M. Zoch, J. Désor, M. Bolte, and C. Krellner, Kagome quantum spin systems in the atacamite family, *Phys. Rev. Materials* **2**, 063402 (2018).
- [S14] W. Sun, Y. X. Huang, Y. Pan, and J. X. Mi, Strong spin frustration and negative magnetization in $\text{LnCu}_3(\text{OH})_6\text{Cl}_3$ (Ln = Nd and Sm) with triangular lattices: the effects of lanthanides, *Dalton Trans.* **46**, 9535 (2017).